

Extranuclear X-ray Emission in the Edge-on Seyfert Galaxy NGC 2992

Edward J. M. Colbert¹

David K. Strickland

*Johns Hopkins University, Department of Physics and Astronomy, Homewood Campus,
3400 North Charles Street, Baltimore, MD 21218*

and

Sylvain Veilleux

University of Maryland, Department of Astronomy, College Park, MD 20742

and

Kimberly A. Weaver

*Laboratory for High Energy Astrophysics, Code 662, NASA/GSFC, Greenbelt, MD 20771;
and Johns Hopkins University, Department of Physics and Astronomy, Homewood
Campus, 3400 North Charles Street, Baltimore, MD 21218*

ABSTRACT

We observed the edge-on Seyfert 1.9 galaxy NGC 2992 with the ACIS CCD array on the Chandra X-ray Observatory, and found several extranuclear ($r \gtrsim 3''$) X-ray nebulae within $40''$ (6.3 kpc for our assumed distance of 32.5 Mpc) of the nucleus. The net X-ray luminosity from the extranuclear sources is $\sim 2-3 \times 10^{39}$ erg s⁻¹ in the 0.3–8.0 keV band. The X-ray core itself ($r \lesssim 1''$) is positioned at $9^h45^m41.^s95 -14^\circ19'34.''8$ (J2000) and has a remarkably simple power-law spectrum with photon index $\Gamma = 1.86$ and intrinsic $N_H = 7 \times 10^{21}$ cm⁻². The near-nuclear ($3'' \lesssim r \lesssim 18''$) Chandra spectrum is best modelled by three components: (1) a direct AGN component from the wings of the PSF, or an electron-scattered AGN component, with Γ fixed at 1.86, (2) cold Compton reflection of the AGN component with intrinsic absorption $N_H \sim 10^{22}$ cm⁻², with approximately the

¹The Catholic University of America, Department of Physics, 620 Michigan Avenue NE, Washington, DC 20064

same 0.3–8.0 keV flux as the direct component, and (3) a 0.5 keV low-abundance ($Z < 0.03Z_{\odot}$) thermal plasma, with $\sim 10\%$ of the flux of either of the first two components. The X-ray luminosity of the 3rd component (the “soft excess”) is $\approx 1.4 \times 10^{40}$ erg s $^{-1}$, or $\sim 5\times$ that of all of the detected extranuclear X-ray sources. We suggest that most ($\sim 75\text{--}80\%$) of the soft excess emission originates from a region between radii of $1''$ and $3''$, which is not imaged in our observation due to severe CCD pile-up. We also require the cold reflector to be positioned at least $1''$ (158 pc) from the nucleus, since there is no reflection component in the X-ray core spectrum. Much of the extranuclear X-ray emission is coincident with radio structures (nuclear radio bubbles and large-scale radio features), and its soft X-ray luminosity is generally consistent with luminosities expected from a starburst-driven wind (with the starburst scaled from L_{FIR}). However, the AGN in NGC 2992 seems equally likely to power the galactic wind in that object. Furthermore, AGN photoionization and photoexcitation processes could dominate the soft excess, especially the $\sim 75\text{--}80\%$ which is not imaged by our observations.

Subject headings: galaxies: spiral—X-rays: galaxies

1. Introduction

Although active galactic nuclei (AGNs) usually dominate the X-ray luminosity in Seyfert galaxies, luminous extranuclear X-ray emission regions (hereafter “EXRs”) extending out to radii of $\sim 10^{2-3}$ pc are fairly common. For example, of the six Seyfert galaxies studied with the ROSAT High Resolution Imager (HRI; spatial resolution $\sim 10''$, energy range 0.2–2.4 keV) by Wilson and collaborators (Wilson 1994), four show spatially extended ($\gtrsim 5''$) soft X-ray emission. In all four cases, the extended X-ray emission is oriented along the same position angle as the nuclear radio structures or the extended narrow-line regions (ENLRs), suggesting a possible connection between the EXRs and the active nucleus. Typical soft X-ray luminosities of the extended emission are $\sim 10^{40}\text{--}10^{41}$ erg s $^{-1}$.

Soft X-ray *spectral* features with similar luminosities were also commonly observed in large-aperture X-ray spectra of Seyfert galaxies, and it is possible that they are in fact the EXRs. In the standard AGN paradigm (e.g., see review by Antonucci 1993), type-1 Seyfert nuclei, which emit a power-law X-ray spectrum, are observed directly (i.e. with little or no absorption), since the line-of-sight to the nucleus is roughly perpendicular to the plane of the obscuring torus. Type-2 Seyfert nuclei are observed at larger angles from the torus symmetry axis, so that the AGN is hidden behind the large absorbing column ($N_H \gtrsim 10^{22}$ cm $^{-2}$) of the obscuring torus. Thus, a power-law model with varying degrees of absorption

serves as a generic “baseline” model for AGN X-ray spectra (e.g. Mushotzky et al. 1980, Mushotzky 1982). However, as shown by Turner & Pounds (1989) and Turner et al. (1991), $\gtrsim 50\%$ of the type-2 Seyfert galaxies observed with EXOSAT and *Einstein* show evidence for surplus X-ray emission in the soft band ($E \lesssim 2$ keV), when the hard-band data are modelled reasonably well with a simple absorbed power-law. This surplus emission is known as “soft excess.”

Since spatially resolved X-ray spectroscopy on arcsecond scales was not possible before the launch of *Chandra*, the origin of the soft excess was not well understood, but some possibilities included (1) X-ray emission from the AGN that “leaks” through holes in the obscuring torus, or possibly around it – the so-called “partial covering” scenario, (2) X-ray emission from the AGN, scattered into our line of sight by electrons along the torus axis, or (3) emission from extranuclear X-ray sources, i.e. EXRs. Since EXRs can be detected with the ROSAT HRI and *Chandra*, it would be useful to know if they are as common as “soft excess,” and, in particular, if there is a direct relationship between the two. In specific cases, this seems to be true. For example, Weaver et al. (1995) conclude that extranuclear X-ray emission observed in a ROSAT HRI image of the Seyfert galaxy NGC 2110 also produces the soft excess that is observed in the total galaxy BBXRT X-ray spectrum.

EXRs in some of the nearest Seyfert galaxies have already been studied with *Chandra* (e.g. NGC 4151: Ogle et al. 2000, Yang, Wilson, & Ferruit 2001; NGC 1068: Young, Wilson & Shopbell 2001; Cyg A: Young et al. 2002; NGC 3516: George et al. 2002; NGC 4388: Iwasawa et al. 2003). The extranuclear X-ray emission generally has a soft ($E \lesssim 2$ keV) spectrum, and is typically spatially coincident with high-ionization optical ENLRs, such as [O III] $\lambda 5007$ nebulae. Their X-ray spectra imply very low abundances ($Z \lesssim 0.1Z_{\odot}$) when fit with a simple one-component thermal plasma model. *Chandra* grating spectra of the brightest regions are well modelled by photoionization and photoexcitation by the AGN (e.g. see Ogle et al. 2003), suggesting there may not be a need at all for collisional excitation (thermal emission) due to a nuclear outflow. Young et al. (2001) conclude that the EXRs in the composite Seyfert-starburst galaxy NGC 1068 are not dominated by starburst phenomena. However, some hot X-ray gas must be produced by the central starburst, and also by any AGN-driven outflows (jets or winds), if they are present. The key is to determine the balance between the outflow and the photoionization/photoexcitation components, since both should be present to some degree.

A more systematic statistical study of EXRs in Seyfert galaxies is needed to understand their nature: wind shocks, jet shocks (e.g. NGC 4258, Cecil, Wilson & de Pree 1995), an expanding hot bubble of gas, or even discrete sources of X-ray emission located outside the nuclear region (e.g. NGC 1068, Wilson et al. 1992). Associating EXRs with the AGN is

tempting, since the AGN can easily both provide enough energy to drive powerful shocks, and provide enough high-energy photons to ionize gas out to kpc-scales. However, many type-2 Seyfert galaxies also have nuclear starbursts that can produce very luminous X-ray point sources (e.g., Fabbiano, Zezas & Murray 2001, Colbert et al. 2004) and drive galactic superwinds that emit diffuse soft X-ray emission (e.g. Heckman 2004, Strickland et al. 2004a,b). By studying the EXRs with the excellent spatial and spectral resolution of Chandra, we can make great progress in understanding the nature of EXRs, and by studying many of them, determine if there is an exact relationship with the very common “soft excess” observed in of Seyfert galaxies. Here we report details from a single deep Chandra ACIS observation of an interesting case study.

We observed the edge-on Seyfert galaxy NGC 2992 with Chandra, since it is known to have a galactic-scale outflow that has been well-studied at many wavelengths: optical (e.g., Colbert et al. 1996a, Allen et al. 1999, Veilleux, Shopbell, & Miller 2001, Garcia-Lorenzo, Arribas, & Mediavilla 2001), near infrared (e.g. Chapman et al. 2000), radio (Ward et al. 1980, Hummel et al. 1983, Colbert et al. 1996b), and X-ray (Colbert et al. 1998). This galaxy has a wide-angled galactic outflow (Veilleux et al. 2001) and a “diffuse” (as opposed to “linear”) sub-kpc radio structure. Since there is heavy obscuration in the nuclear region, it is difficult to tell whether NGC 2992 has a strong nuclear starburst or not. The galactic outflow in NGC 2992 may be quite different from those in Seyfert galaxies that have already been observed with *Chandra* (e.g. NGC 2110, M51, and NGC 4151), which have “linear” nuclear radio structures. Understanding its origin of the EXRs and the outflows may offer important clues to the “starburst-AGN connection.” Since NGC 2992 has very well studied ENLRs and also has a kiloparsec-scale outflow, it is an ideal galaxy to study with Chandra.

In Figure 1, we show a *V*-band image of NGC 2992 and its companion galaxy NGC 2993. This interacting pair is also known as Arp 245. A comprehensive multi-wavelength study of the interacting system is presented in Duc et al. (2000). NGC 2992 has morphological type Sab, while NGC 2993 has type Sa (Sandage & Bedke 1994). The projected separation between the two galaxies is $\sim 3'$ (28 kpc, assuming a distance¹ of 32.5 Mpc). Optically luminous tidal plumes extending from both galaxies are evident in deep optical images (e.g. Sandage & Bedke 1994, Duc et al. 2000), and some evidence of them can be seen in Figure 1.

We describe the observations and data reduction in section 2, and give results in section 3. An interpretation of the X-ray emission as starburst-driven and AGN-driven winds are

¹Assuming a Hubble constant $H_0 = 71 \text{ km s}^{-1} \text{ Mpc}^{-1}$ (Spergel et al. 2003) and a recessional velocity of 2311 km s^{-1} (Keel 1996), NGC 2992 is located at a distance of 32.5 Mpc, so that $1''$ corresponds to 158 pc.

given in section 4.

2. Observations and Data Reduction

The edge-on Seyfert galaxy NGC 2992 and its companion NGC 2993 were observed with the Chandra X-ray Observatory (CXO) in the AO4 cycle, on UT dates 16–17 February 2003 (Obs. ID 3956). The ACIS-S CCD array was used, and the pointing center was chosen such that the two galaxies were centered in the back-illuminated S3 chip (CCD 7). As a result, the off-axis angle of the nucleus of NGC 2992 was $3.'26$. The satellite roll angle was constrained to 353° so that the CCD readout column would be oriented along the major axis of NGC 2992, and the anticipated readout “streak” (due to the very bright nuclear point source) would not interfere with X-ray emission extending along the galaxy minor axes. The total on-source EXPOSURE time of the level-1 events file was 50.23 ks, using a CCD frame time of 3.2 s. The CCD temperature during the observation was -120° C.

The level-1 events data were re-processed with the `ACIS_REPROCESS_EVENTS` script using the CXO data reduction software package CIAO v3.0.2, and Chandra calibration database CALDB v2.26. No CTI correction was performed due to pile-up effects of the nuclear source. After re-processing, the filtered level-2 events had a total EXPOSURE time of 49.54 ks. Two separate level-2 event files were created. The first was made using the normal event filtering (i.e., keeping those events with “good” ASCA event grades of 0, 2, 3, 4, and 6). This standard filtering is appropriate for unpiled events, but piled events tend to migrate from “good” grades to “bad” grades (see Chandra POG²), so we created another level-2 event file for photons with all event grades. The second events file is *only* used to illustrate which pixels near the X-ray core are contaminated by pile-up (see section 3.1.1).

Spectra were extracted from the first (“good”) level-2 event file for various regions using the CIAO `ACISSPEC` script (v3.2), which creates weighted ancillary response files (ARFs) and response matrix files (RMFs) for extended spatial regions.

²The Chandra Proposer’s Observatory Guide (POG), <http://asc.harvard.edu/proposer/POG>

3. Results

3.1. Spatial Analysis

In Figure 2, we show several images of the large-scale X-ray emission from NGC 2992/3. In 1992 and 1994, soft (0.2–2.4 keV) X-ray emission was detected from both galaxies with the ROSAT High-Resolution Imager (HRI) instrument (Figure 2a). For comparison with the HRI image, we constructed a soft X-ray image from the ACIS data, using photons with energies 0.3–2.4 keV (Figure 2b). The readout streak, due to CCD pile-up from the very bright X-ray nucleus of NGC 2992, is clearly seen in the ACIS images.

3.1.1. X-ray Point Sources

In addition to the very bright nucleus of NGC 2992, we detect twenty³ X-ray point sources in the ACIS CCD that includes the NGC 2992/3 complex. We list X-ray properties of the twenty point sources in Table 1, and display the positions of the sources nearest to NGC 2992/3 in Figure 3. There are four sources within the R_{25} ellipses of the two galaxies: source 7 ($L_X \approx 10^{39}$ erg s⁻¹) is 17'' (2.7 kpc) southeast of the nucleus of NGC 2992, and sources 9, 10, and 11 ($L_X \approx 5 \times 10^{39}$ erg s⁻¹) are all within $\sim 10''$ (1.6 kpc) of the center of NGC 2993. There are three other sources within ellipses corresponding to $R=2R_{25}$: source 5 (NGC 2992), and sources 8 and 13 (NGC 2993).

3.1.2. Position of the X-ray Nucleus

The X-ray point source in the nucleus of NGC 2992 is obviously the dominant source of X-ray emission. Its X-ray luminosity of $\sim 10^{42-43}$ erg s⁻¹ (e.g. Gilli et al. 2000) indicates that the emission is most likely coming from the Seyfert nucleus (Ward et al. 1980). We determined the position of the X-ray core using two independent methods. We first fit elliptical isophotes to the full-band X-ray image of the nuclear source, using the ELLIPSE

³The twenty sources were detected by the XASSIST (see URL www.xassist.org) data reduction package. XASSIST first identifies a larger list of sources using the CIAO WAVDETECT program. These WAVDETECT sources are then rigorously tested using image fitting of a Gaussian model with a sloping background. Those sources that pass the spatial fitting test and have a signal-to-noise (S/N) ratio > 2.0 are then kept. Here, S/N is $N(src)/\sqrt{N(bck) \times A(src)/A(bck)}$, where N and A are the number of counts and areas for the source and background regions. For CCD 7, this S/N ratio corresponds to $\sim 3.5 \times 10^{-15}$ erg s⁻¹ cm⁻².

task in STSDAS v3.2 (with IRAF v2.12.2). Next, we obtained very accurate constraints for one dimension of the X-ray position by finding the centroid of the CCD readout streak.

The X-ray nucleus of NGC 2992 is positioned off-axis by $\approx 3.26'$, so that the ACIS point-spread function is asymmetric, and approximately elliptical. In the top two panels of Figure 4, we show grayscale maps of the raw X-ray counts for all (“good” and “bad”) event grades, and also for just the “good” event grades (see section 2). Grade-migration due to pile-up is not noticeable in the lowest three contours 30, 60, and 90 counts pixel⁻¹, where the pixel size is 0.492”), but is very noticeable at the fourth contour level (120 counts pixel⁻¹). For comparison, the three ellipses in Figure 4d are for best-fit surface brightnesses of 52, 75, and 110 counts pixel⁻¹.

The centroiding uncertainty for each of the three ellipses, as reported by the ELLIPSE routine, is very small (≈ 0.1 pixel, or $\sim 0.05''$). The three positions differ by $\lesssim 0.25''$, and we assume this to be the net uncertainty of this method. In Figure 4d, we show three $r = 0.25''$ circles, labeled *A*, *B*, and *C*, for the inner, middle, and outer ellipses, respectively. Crosses are marked centers of the three circles.

As mentioned, we also used the readout streak in the ACIS image to constrain the position of the X-ray core. For very bright X-ray point sources, a significant number of events are detected during the very brief CCD readout of the CCD (40 μ s of each 3.2 s frame; see Chandra POG). At the end of the readout time, these events are left scattered along the CCD column of the X-ray point source. By rotating our ACIS image by the roll angle (7.05°) and finding the best-fit image column for the center of the readout streak, we were able to construct a line in the original (unrotated) image that accurately estimates one linear dimension of the position of the X-ray core (see Figure 4, lower two panels). We used IRAF IMEXAMINE to fit Gaussian profiles across the streak, for positions ≈ 30 –100” above and below the X-ray point source. The standard deviation for the best-fit column values was 0.3 pixels. As can be seen in the lower left panel of Figure 4, both our ellipse fitting and our readout streak method give consistent results.

A position mid-way between the three ellipse centroids and the readout streak marks our best estimate for the position of the NGC 2992 X-ray peak ($9^h 45^m 41.95^s -14^\circ 19' 34.8''$ [J2000]). This position was estimated by eye; however, the uncertainty is a fraction of a pixel. We mark this position with a diamond symbol in Figure 4d. The estimated nominal uncertainty in absolute astrometry for Chandra is $\approx 0.5''$ (e.g., Aldcroft 2002). Thus, we also show an error circle for the position of the X-ray core, as a dashed circle of radius 0.5”. In section 4, we compare our measured position of the X-ray core with positions of features in other wavebands.

3.1.3. Near-nuclear X-ray Emission

Here we concentrate on extra-nuclear emission within $\sim 10''$ of the X-ray nucleus of NGC 2992 ($\lesssim 1.58$ kpc at a distance of 32.5 Mpc). In Figure 5, we show grayscale plots of the near-nuclear X-ray emission in four different energy ranges: very soft (0.3–0.5 keV), soft (0.3–1.0 keV), hard (4.0–8.0 keV), and full-band (0.3–8.0 keV). We also show a smoothed image of the CHART/MARX PSF in the full band, and compare it with a smoothed image of our full-band ACIS observation. The slight elongation of the PSF along PA $\sim 45^\circ$ is due to the source being off-axis by $\sim 3.3'$. This elongation is noticeable in all of the full-band images, and in the hard-band image. There is no obvious extended (i.e., asymmetric with respect to the elongated PSF) hard X-ray emission (Figure 5e), but there *is* extended (asymmetric) soft X-ray emission from ~ 2 – $4''$ (0.3–0.6 kpc), toward the SE (see Figures 5c and 5f). Throughout the rest of the paper, we refer to this extended X-ray source as source ‘SE.’

Due to the severity of the CCD pile-up $\lesssim 2.5''$ (see section 3.1.2), estimating the flux of this extended soft X-ray source within $\sim 2.5''$ is not straightforward. The total number of 0.3–1.0 keV counts between 2.5 and 5.0'' is 242 ± 16 , 360 ± 19 , 126 ± 11 , and 60 ± 8 for the four quadrants 1– 90° , 91– 180° , 181– 270° , and 271– 360° , respectively. Under the assumption that the first and fourth quadrants are background plus AGN contamination, source SE (i.e., the second and third quadrants) has ~ 100 – 200 net counts in the 0.3–1.0 band. This equates to an observed 0.3–8.0 keV luminosity of ~ 1 – 2×10^{39} erg s $^{-1}$ for a 0.5 keV bremsstrahlung model with Galactic absorption.

Using the *Einstein* HRI ($E \approx 0.1$ – 3.5 keV), Elvis et al. (1990) claimed to detect extended emission within a radius of $10''$, with an X-ray luminosity of $\approx 4 \times 10^{41}$ erg s $^{-1}$ (adjusted for our distance, and using a 0.25 keV Bremsstrahlung model with Galactic absorption). The *Einstein* emission was detected in the quadrant centered at PA $\sim 23^\circ$, but no emission was found in the other three quadrants. Since this conflicts with our Chandra results, we suggest that the *Einstein* detection was either due to a variable X-ray source, or was spurious.

3.1.4. Kiloparsec-Scale X-ray Emission

Next, we investigate extended X-ray emission on scales $\gtrsim 10''$ ($\gtrsim 1.6$ kpc at 32.5 Mpc). To investigate the presence of any extended emission in our Chandra image, we computed X-ray counts in radial bins as a function of angle. We used eight 45° angular wedges with the first octant starting at PA -15.5° (see Figure 6). Octants 1 and 5 were centered on the

CCD readout streak and were ignored in the rest of the analysis.

We modelled the PSF of the X-ray core in a number of different ways, none of which were ideal. We first tried to simulate the PSF with the Chandra Ray Tracer⁴ (ChaRT), using the spectrum of the X-ray core (section 3.2.1) as an input model. The ChaRT simulation was performed with the same off-axis angle and telescope roll angle as our ACIS observation. The output SAOSac ray-tracing files were converted to event files with the MARX⁵ Chandra simulator. We plot radial profiles for the CHART/MARX PSF in Figure 6a. The background level (0.1 counts pixel⁻¹) was added to the CHART/MARX PSF. While this experiment was useful to show that no large-scale azimuthal variation is expected for our observational parameters, the CHART/MARX PSF falls off more steeply than the data for all octants (see Figure 6a; see also Smith, Edgar & Shafer 2002). We attribute this difference to the fact that MARX does not account for aspect dither, which makes the simulated PSF narrower than the actual one (K. Ishibashi, priv. comm.).

We first tried to use radial profiles from three octants that appeared free of excess emission (regions 2, 6 and 8 in Figure 6b). We found no significant excess emission for hard X-ray emission with energies ≥ 2.5 keV, but did find excess emission in the softer bands. We first analyzed the “ROSAT” band from 0.3–2.4 keV, and later experimented with smaller energy ranges in the soft band, and with harder bands. Octant 6 appeared to have some possible excess X-ray emission, so we downgraded our radial profile to include only octants 2 and 8, both of which did not show significant excess after subsequent PSF subtraction (see Figure 6d). The most significant excess extends eastward along PA $\sim 190^\circ$, out to $\sim 40''$, roughly perpendicular to the galaxy disk (see Figure 6c). Using the combined radial profiles from regions 2 and 8 for a PSF, we calculate an excess of 90 ± 22 X-ray counts in this octant, from 20–40'' (3.2–6.3 kpc). We found three other regions which had significant ($>3\sigma$) excess over our model PSF (see Figure 6d): a point-like source in region 4 (source 7 in Table 1) with 82 ± 19 counts (from 15–25''), diffuse emission with 75 ± 22 counts in region 6, from 15–30'', and an extended source nearer to the nucleus (region 7, 10–20''), with 74 ± 24 counts.

We then constructed an image from our model PSF and subtracted it from from the Chandra image to show the structure of these sources (see Figure 6d). The 0.3–2.4 keV Chandra image was first smoothed with a Gaussian kernel of $\sigma = 1.5''$. The PSF was scaled by trial and error so that after subtraction, the net counts for extra-nuclear regions within $\sim 2'$ were zero. This was done by examining radial and horizontal cuts across the image and ensuring that the pixel values in source-free regions far away from the nucleus fluctuated

⁴URL <http://cxc.harvard.edu/chart>

⁵URL <http://space.mit.harvard.edu/CXC/MARX>

about 0.0 counts pixel⁻¹. For comparison, we also show the (unsubtracted) 0.3–2.4 keV Chandra image Figure 6b.

No excess emission was found from our radial profile analyses of the hard (2.4–8.0 keV) X-ray emission. While not enough counts were typically available in narrow energy bands, we did notice that the point-like source in region 4 (point source 7 in Table 1) was significantly harder than expected for thermal plasma emission with kT of $\lesssim 1$ keV, with a significant number of photons with $E \gtrsim 1.5$ keV. We list excess counts in several other energy bands in Table 2. Since the angular breaks that define our octants often pass through well-defined X-ray sources, we also list X-ray counts and 0.3–2.4 keV luminosities for the most well-defined clumps in the PSF-subtracted image. These sources are labelled $e3a^*$, $e3b$, $e6^*$, and $e7^*$ in Table 2, and their defining regions are shown in Figure 9. Those sources with an asterisk fall outside the angular range defined by their octants: for example, $e7^*$ is primarily in octant 7, but also extends into octant 6.

3.2. Spectroscopy

3.2.1. Nuclear Source

We extracted a spectrum of the X-ray core from the CCD readout streak following a prescription from the CXO calibration team (R. Smith, priv. comm.). We note here that the events in the readout streak do not suffer from CCD pile-up. Source photons from the readout streak were taken from two thin rectangular regions extending ~ 0.75 – $4'$ above and below the nuclear source. Background counts were subtracted, using four thin rectangular regions, one both sides of the readout streak. Ancillary Response Files and Response Matrices were generated for a small circular region enclosing the X-ray core. The source spectrum was then grouped so that it had a minimum of 20 counts per spectral bin. Since the fraction of the total counts that are detected in the streak is not well calibrated, the absolute normalization obtained from spectral fitting is not useful. However, the shape of the spectrum is very useful.

Restricting the energy range to 0.3–8.0 keV, we obtain a spectrum with 6744 source counts. We use XSPEC v11.3.0 for spectral fitting. An external Hydrogen column was fixed at the Galactic value of 5.26×10^{20} cm⁻² (Dickey & Lockman 1990). An additional intrinsic Hydrogen column was allowed to vary during the fit. With a simple absorbed power-law model, we obtain a very good fit ($\chi^2/dof = 197.0/205$), with a power-law model

with $\Gamma = 1.86 \pm 0.08^6$, and $N_H = 0.71 \pm 0.05 \times 10^{22} \text{ cm}^{-2}$. Adding a neutral ($E = 6.4 \text{ keV}$) Fe $K\alpha$ line as a Gaussian line only improves the fit by $\Delta\chi^2 \approx 0.2$.

This power-law slope is consistent with the 1997–1998 large-aperture SAX spectrum ($\Gamma \approx 1.7$; Gilli et al. 2000), but is not consistent with the much flatter ASCA spectrum taken in 1994 ($\Gamma \approx 1.2$; Weaver et al. 1996). Photon indices of $\Gamma \approx 1.9$ are typical in type-1 Seyfert nuclei (e.g. Nandra & Pounds 1994; Nandra et al. 1997), where the X-ray AGN is viewed directly. Since we know the X-ray core streak spectrum comes from a very small region $\approx 1\text{--}2$ pixels across ($\approx 75\text{--}150 \text{ pc}$), and its spectrum is not consistent with Compton reflection, we conclude that it must be either emission directly from the AGN, as in type-1 Seyfert galaxies, or gray scattering of the AGN emission from electrons within $\sim 150 \text{ pc}$ ($\approx 1''$) of the AGN. In the next section, we assume the direct spectrum of the AGN is given by the streak spectrum, and use this to constrain the AGN component of the spectrum within $\sim 3 \text{ kpc}$ of the nucleus.

3.2.2. Near-Nuclear X-ray Emission

Using the ACISSPEC CIAO tool, we extracted a spectrum of the X-ray emission within a radius of $18''$ (2.8 kpc), centered on the X-ray core (see section 3.1.2). We excluded the very central region (with piled events) by rejecting all events within the “middle” ellipse in the lower left panel of Figure 4 (semi-major and semi-minor axes $3.4'' \times 2.7''$). We also excluded events from a faint point source (source 7, Table 1), and from a thin rectangular region enclosing the CCD readout streak. This extraction region thus includes a fraction of the X-ray core (section 3.1.2), all of source SE (section 3.1.3), some of the emission from extended sources e6 and e7 (section 3.1.4), and the accumulation of any other “undetected” extended X-ray sources within 2.8 kpc of the nucleus. Background counts were taken from four remote source-free rectangular regions adjacent to the nuclear region. The $\approx 14,600$ -count $0.3\text{--}8.0 \text{ keV}$ source spectrum was binned to $>20 \text{ counts bin}^{-1}$ and analyzed with XSPEC. We list the results from spectral fitting in Table 3. All models include an additional neutral Hydrogen absorption component, fixed at $5.26 \times 10^{20} \text{ cm}^{-2}$ (Galactic value from Dickey & Lockman 1990). Since much of the emission from the AGN point-source has been rejected due to pile-up and much of the remaining emission has been omitted by our extraction region, the absolute fluxes we obtain from the AGN spectral components are not useful for comparison with previous results (e.g. ASCA).

The near-nuclear spectrum is fairly well fit ($\chi^2_\nu = 1.13$) by a shallow ($\Gamma \approx 0.9$) absorbed

⁶Unless otherwise specified, all errors are for 90% confidence for one degree of freedom ($\Delta\chi^2 = 2.7$).

power-law. However, since some of the photons in source region are from the PSF wings of the X-ray core ($\Gamma = 1.86$; section 3.2.1), we must reject this simple model.

We thus included a power-law component with the slope fixed at $\Gamma = 1.86$, which was the value determined from the spectrum of the CCD readout streak (i.e. one or two pixels from the X-ray core). Since the PSF wings from the X-ray core will contribute in our near-nuclear region ($r > 18''$), a $\Gamma = 1.86$ power-law component should be present. The absolute normalization of the streak spectra is not well calibrated (R. Smith, priv. comm.), so we left the normalization to the $\Gamma = 1.86$ power-law free while fitting. We did not correct for the difference in the PSF wings for soft and hard energies (e.g., Allen et al. 2004), but we note that the PSF wings are quite similar for energies ~ 4.0 – 8.0 keV, and this is the energy range for which much of the events from the power-law component reside.

A simple absorbed power-law, with Γ and N_H fixed at the same values as for the X-ray core, is a very poor fit ($\chi_\nu^2 \approx 3.7$). However, if a second absorbed power-law is added (“partial covering”), a good fit ($\chi_\nu^2 = 1.05$; $\chi^2/\nu = 372/354$) is obtained, with $\Gamma \approx 0.5$, and $N_H \sim 10^{20}$ cm $^{-2}$ for the second component. In this model, the flat power-law component has an observed 0.3–8.0 keV flux ~ 2.5 times that of the first (AGN) component. While we do not view this partial covering model as physically reasonable, it does show the importance of components other than direct or electron-scattered AGN emission.

If the second component is replaced with a MEKAL thermal plasma model, the fit is very poor: $\chi_\nu^2 \approx 2.8$, for either fixed (solar) or variable abundances (best fit at $Z \approx 0.1Z_\odot$).

We next tried a cold reflection model (PEXRAV) for the second component, fixing the input power-law spectrum at $\Gamma = 1.86$. This is again a fairly good fit ($\chi_\nu^2 = 1.18$), although it is still significantly poorer than the partial covering model, with a $\Delta\chi^2$ of 37.

Adding a third component to the fit (a Mekal thermal plasma model) significantly improves the fit ($\chi_\nu^2 = 1.03$). Our best fit model (PL+PEXRAV+Mekal, see Table 3, model 3b) is obtained for a low-abundance plasma with $kT \approx 0.5$ keV and $Z \approx 0.01Z_\odot$. Note that the best-fit PEXRAV components are almost completely reflection-dominated, i.e. they have very large R values. We discuss the issue of low abundances further in section 4.2.3. Compared with the partial-covering model, χ^2 is lower for this model by a difference of 10. We take model 3b as our best model and measure observed 0.3–8.0 keV luminosities of 2.3×10^{41} erg s $^{-1}$ for the reflected component, and 1.4×10^{40} erg s $^{-1}$ for the “thermal” component. In Figure 7, we show the near-nuclear spectrum, together with the various model components.

We find no evidence for an Fe K line in the near-nuclear spectrum. If we add in a Gaussian line fixed at 6.4 keV to model 1a, 1b (fixed PL models), or our best-fit model (3b),

an equivalent width ≈ 50 eV line is fit best, but $\Delta\chi^2 \lesssim 1$. Although our proposed reflection component in the near-nuclear spectrum may well produce a strong Fe K line, there is also significant direct AGN emission in the composite spectrum. For example, for our best-fit model (3b), $\sim 50\%$ of the 0.3–8.0 keV flux comes from the direct (PL) component (see Table 3). Thus, any Fe K line emission produced by cold Compton reflection may just be washed out. To test this hypothesis, we used a single PEXRAV model with $\Gamma = 1.86$ for the AGN component, and added a narrow Gaussian line fixed at 6.4 keV. The fit was quite reasonable ($\chi^2 = 378.1$) compared with other models in Table 3. The best-fit value of R was 15.87. The Gaussian line was best fit with an equivalent width of 24 eV and an upper limit ($\Delta\chi^2 = 2.7$) of 674 eV. If only the reflection component is allowed by the PEXRAV model, the equivalent width increases by a factor of 1.63. Therefore, the upper limit one would expect if the direct component was not present is ~ 1.1 keV, which is more consistent with a reflection-dominated X-ray spectrum.

3.3. Properties of the Soft Excess Emission

As mentioned in section 3.1.4, the extended X-ray sources e6 and e7 with net 0.3–8.0 keV luminosity $L_X = 1.2 \times 10^{39}$ erg s $^{-1}$ (Table 2) comprise part ($\sim 10\%$) of the “thermal” soft excess ($L_X \approx 1.4 \times 10^{40}$ erg s $^{-1}$), as does the source SE with $L_X \sim 1\text{--}2 \times 10^{39}$ erg s $^{-1}$ (section 3.1.3). It is quite possible that the unaccounted ($\sim 75\text{--}80\%$) soft excess emission could be explained by undetected or unresolved hot, extranuclear gas clouds, although diagnosing this with the existing ACIS data is not very practical, due to the strong X-ray core and uncertainties in the PSF. Since the AGN core spectrum extracted from the readout streak does not show any evidence for soft excess, an alternative explanation is that the unaccounted soft excess originates from very luminous ($L_X \sim 10^{40}$ erg s $^{-1}$) EXRs in the region between $\approx 1\text{--}2.5''$. A fraction of these photons would then be repositioned to larger radii by the Chandra PSF and so would have been included in our near-nuclear spectrum ($r \gtrsim 3''$).

4. Discussion

As we have shown, we detect $\sim 2\text{--}3 \times 10^{39}$ erg s $^{-1}$ of extended soft X-ray emission in NGC 2992, and find evidence for $\sim 1 \times 10^{40}$ erg s $^{-1}$ in a “low-abundance thermal” spectral component. The AGN nucleus ($r \lesssim 1''$) is well fit by a power-law, but a larger aperture spectrum of the near-nuclear region requires a significant cold reflection component.

In this section, we discuss possible scenarios for the emission processes producing the

X-ray emission from the nuclear source, the extended sources e3, e6, e7 and SE, and the soft excess.

4.1. The Nuclear Point Source

Large-aperture 2.5' ASCA observations of the X-ray nucleus in 1994 by Weaver et al. (1996) yielded similar *observational* results to our near-nuclear model 1a (i.e., when both datasets are modelled with a simple absorbed power law; $\Gamma \sim 1$ and $N_H \sim 2 \times 10^{21} \text{ cm}^{-2}$). This *observational* model is obviously an inadequate description of the emission components, but it shows general similarity in the spectral shape. Weaver et al. model the ASCA spectrum with both Compton reflection and gray scattering (partial-covering model) of a $\Gamma = 1.7$ nuclear source that was hidden behind an absorbing column of $\sim 10^{22} \text{ cm}^{-2}$. However, BeppoSAX observations in 1997 and 1998, with a similar aperture, were well fit by a simple power-law model with $\Gamma \approx 1.7$ and $N_H \approx 10^{22} \text{ cm}^{-2}$ (Gilli et al. 2000). Thus, as shown by Weaver et al. (1996), the cold (Compton) reflection component is historically variable on the scale of a few years.

The fact that we do not see evidence for cold reflection in the nuclear streak spectrum but we do see evidence for it in the near-nuclear ($r \gtrsim 3''$) spectrum implies that the reflection region is located outside of the 1–2 pixels that are clocked along the readout streak. Thus, we argue that the cold reflection region is located at radii $r \gtrsim 0.5\text{--}1.0''$, or $r \gtrsim 75\text{--}150 \text{ pc}$.

We show the positions of the X-ray core in optical and radio images of the nuclear region in Figure 8. The V-band, $H\alpha$, and [O III] peaks (panels a, b, and d) are displaced from the X-ray core position by 1–2'' to the northwest. This displacement could be an obscuration effect, or it could be due to alignment uncertainties between the optical and X-ray frame. Unfortunately, CCD pile-up prevents reliable imaging of any of the ACIS X-ray emission near the peak of the NW “ionization cone” (i.e., the NW $H\alpha$ and [O III] peak) and we cannot diagnose if there is another X-ray source there, such as the cold reflector. Veilleux et al. (2001) and Garcia-Lorenzo et. al (2001) find that the stellar kinematic center is positioned $\approx 1''$ *southwest* of the [O III] peak. Thus, the supermassive black hole, as marked by the X-ray and radio core, may not yet have settled into the center of the galaxy. However, since gas motions are quite complex in the center of NGC 2992 (e.g., Veilleux et al. 2001), and the galaxy disk is viewed nearly edge-on, perhaps the X-ray/kinematic center displacement is consistent with uncertainties in modelling the optical data.

The X-ray core is, however, coincident with the 6 cm radio core – the apex of the two diffuse “radio bubbles”, a.k.a. “figures-of-eight” (see Figure 8c). This suggests that the radio

bubbles may be inflated by the AGN (e.g. Wehrle & Morris 1988), and not a starburst, since NIR observations suggest that the youngest star-forming region is located in the dust lane (Chapman et al. 2000), a few arcseconds northwest of the X-ray core and the radio core.

4.2. Extended X-ray Emission and Soft Excess

4.2.1. Near-nuclear X-ray Sources

The diffuse soft X-ray emission within $5''$ is displayed against the optical and radio emission in Figure 8. The SE X-ray source, which has a centroid along PA $\sim 160^\circ$, is coincident with the SE radio bubble, but there is no luminous optical line or continuum emission there. It is thus possible that the X-rays from the SE source are collisionally excited emission produced by outflowing gas in the bubble. The apparent “low abundance” of this X-ray gas is discussed in section 4.2.3.

Allen et al. (1999) and Veilleux, Shopbell, & Miller (2001) find very high velocities for the ENLR gas in the SE cone, as high as 670 km s^{-1} (Allen et al. 1999). Shock-model fits to the emission line ratios from that region imply shock velocities of $\sim 300\text{--}500 \text{ km s}^{-1}$ (Allen et al. 1999). A shock velocity of 500 km s^{-1} will produce thermal X-rays with temperature $\approx 0.3 \text{ keV}$, which is certainly consistent with the results from our spectral fitting ($kT = 0.3\text{--}0.8 \text{ keV}$, model 3b, Table 3).

Based on kinematic modelling of the $\text{H}\alpha$ -emitting gas, Veilleux et al. (2001) estimate a kinetic energy luminosity of $L_{KE} \approx 10^{40} (n_e/100 \text{ cm}^{-3})^{-1} \text{ erg s}^{-1}$. Starburst-driven winds yield X-ray luminosities of $\approx 0.03 L_{KE}$ (e.g. Strickland 2004), implying $\sim 3 \times 10^{38} \text{ erg s}^{-1}$ of soft X-rays from the nuclear outflow in NGC 2992. This is an order of magnitude lower than L_X of the SE X-ray source; however, since $L_X \propto n_e^2 \phi$, where n_e is the electron density and ϕ is the volume filling factor, it is possible that the physical conditions in the SE region could produce a significantly larger X-ray luminosity in NGC 2992.

Compared with typical ENLR gas, the hot X-ray emitting gas is quite tenuous. Assuming a $0.2\text{--}2.4 \text{ keV}$ emissivity of $10^{-22.4} \text{ erg cm}^3 \text{ s}^{-1}$ (Suchov et al. 1994), we derive gas densities $n \sim \phi_X^{-1/2} \times (0.3\text{--}2) \times 10^{-2} \text{ cm}^{-3}$ for the four well-defined X-ray sources in Table 2 (*e3a**, *e3b*, *e6**, and *e7**; see Colbert et al. 1998 for detailed description of similar calculations). Here ϕ_X is the volume filling factor of the X-ray emitting gas, and is distinct from ϕ for the optical line emitting gas. ENLR clouds have much larger electron densities: $\sim 10^{2-4} \text{ cm}^{-3}$ (e.g. Robinson 1989, 1994). The implied pressure $p = 2nkT$ of the X-ray gas, assuming $kT=0.5 \text{ keV}$ (as in Table 2), is $p \sim \phi_X^{-1/2} \times (0.5\text{--}3) \times 10^{-11} \text{ dyne cm}^{-2}$, which is reasonably close to $n_e kT$ of ENLR clouds, suggesting there may be pressure equilibrium be-

tween the two gas phases. The cooling-time of the X-ray gas can also be estimated (cf. Colbert et al. 1998), and we find $t_{cool} \sim \phi_X^{+1/2} \times (3-20) \times 10^7$ yr.

4.2.2. Kiloparsec-scale X-ray Sources

As mentioned in section 3.1.4, we find three diffuse extranuclear X-ray sources (e3, e6 and e7), each with $L_X \approx 6 \times 10^{38}$ erg s⁻¹ (Table 2). These sources are located at larger distances ($r = 10-40''$, or 1.6–6.3 kpc; see Figure 6d). In Figure 9, we show the relative positions of these sources with respect to the kpc-scale optical and radio emission. We also label the well-defined X-ray clumps in the image as e3a*, e3b, e6*, and e7* (see section 3.1.4).

A kpc-scale 20 cm radio “arm” extends eastward from the nucleus in the same PA as source e3, and reaches the inner part of this X-ray source. Thus both could be generated by a kpc-scale nuclear outflow. Source e3 is also positioned within the opening angle of the SE ionization cone (see Figure 9d), and thus AGN photoionization is also a possible emission mechanism.

4.2.3. Soft Excess

As summarized by Ogle et al. (2003), many of the extended X-ray sources found in Seyfert galaxies are well modelled with pure photoionization and photoexcitation models — collisional excitation is not required. The characteristic observational spectral signature of soft excess in non-grating Chandra and XMM observations is a one- or two-temperature thermal model *with near-zero abundances* (e.g. Bianchi et al. 2003, Schurch et al. 2002, Done et al. 2003), which is precisely the same as our results for NGC 2992. The spectra of the brightest extranuclear X-ray nebulae in NGC 1068 and NGC 4151 are well fit by AGN photoionization and photoexcitation models, with no need for collisional excitation (e.g. Sako et al. 2000, Sambruna et al. 2001, Kinkhabwala et al. 2002, Ogle et al. 2003). However, the exact same “low-abundance” phenomenon occurs for X-ray emission from starburst-driven superwinds when they are fit with a one-temperature thermal model (e.g. Ptak et al. 1997). A high-quality grating spectra of the starburst galaxy M82 is much better represented with multi-temperature abundances (Read & Stevens 2002). Strickland et al. (2004a,b) find that a *physically reasonable* solution for Chandra CCD (non-grating) spectra of superwinds is a two-temperature model with low Fe abundances. Thus, the low metallicity implied by our simple single-temperature “thermal plasma” component (e.g. model 3b, Table 3) does not necessarily imply that the soft excess (which includes e3, e6, e7 and SE) is produced solely

(or even partially) by AGN photoionization. The result is ambiguous.

4.3. AGN-driven Outflow *vs.* Starburst-driven Outflow

Does NGC 2992 have a nuclear starburst that could indeed power a galactic wind? It has a total FIR luminosity of $7 \times 10^{43} \text{ erg s}^{-1}$ (Moshir et al. 1997), which suggests a SFR of $\approx 4 M_{\odot} \text{ yr}^{-1}$, assuming the FIR emission from the AGN can be neglected and the $\text{SFR} = 5.7 \times 10^{-44} L_{\text{FIR}}$ (cf. Colbert et al. 2004). The IRAS colors of NGC 2992 are more similar to those of starbursts than to “pure” (not composite starburst-Seyfert) Seyfert galaxies (e.g., Colbert 1997). Strickland et al. (2004b) show empirically that X-ray halo emission from a starburst $L_{\text{halo}} \approx 4 \times 10^{-5} L_{\text{FIR}}$, which suggests NGC 2992 should emit $\approx 3 \times 10^{39} \text{ erg s}^{-1}$ in soft X-rays from the hypothetical $4 M_{\odot} \text{ yr}^{-1}$ starburst. Based on the range in $L_{\text{halo}}/L_{\text{FIR}}$ for the starburst galaxies studied by Strickland et al. (2004b), the starburst wind component could be as much as a factor of 2 more: $L_{\text{halo}}^{\text{max}} \approx 6 \times 10^{39} \text{ erg s}^{-1}$. This is certainly consistent with the 20–25% of the soft excess that we image with Chandra ($L_{\text{X}}^{\text{net}} \approx 3\text{--}4 \times 10^{39} \text{ erg s}^{-1}$ from sources e3, e6, e7, and SE).

However, detecting a nuclear starburst in NGC 2992 is difficult, due to heavy obscuration and the bright X-ray AGN. It is quite possible that the outflow (and thus the extranuclear X-ray sources) may be energized by the AGN instead. Soifer et al. (2004) find that $\approx 50\%$ of the $12\mu\text{m}$ IRAS emission from NGC 2992 is positioned within $0.''34$ (50 pc) and conclude that this compact $10\mu\text{m}$ emission is produced by an AGN instead of by a nuclear starburst. It is not clear, however, if this is also true of the higher wavelength IRAS fluxes (e.g. $60\mu\text{m}$ and $100\mu\text{m}$), which are usually used to estimate the star-formation rate of the putative starburst. The FIR/radio flux ratio μ for NGC 2992 is quite low (2.09), compared with starburst galaxies, for which μ clusters tightly near 2.5 (cf. Colbert et al. 1996b), suggesting significant AGN radio emission. Thus, the radio loops may be more consistently explained by an AGN-driven outflow. Chapman et al. (2000) do, however, find very red ($R - H$ as high as 4.8) “starburst” regions within $\sim 1''$ of the NIR core, in the dust lane. Hence, it is possible that a strong starburst does exist, but remains hidden behind the dust lane (e.g. see V-band image in Figures 8a and 9c).

It is certainly possible that AGN photoionization could be powering the 75–80% of the soft excess that was *not* imaged in our Chandra observations. For example, this emission could be positioned closer ($r \lesssim 5''$) to the AGN and thus invisible in the Chandra image due to pile-up effects and/or the tremendous intensity of the AGN X-ray core.

We are grateful to Randall Smith, Tahir Yaqoob, Steve Kraemer, and Patrick Ogle for

helpful discussions, and to B. Garcia-Lorenzo, M. Allen and P. Shopbell for providing images and data analysis tools. We thank the anonymous referee for helpful suggestions. EJMC acknowledges support from NASA for SAO grant GO3-4116X.

REFERENCES

- Aldcroft, T. 2002, (Cambridge: Chandra X-ray Science Center)
- Allen, C. L., Jerius, D., & Gaetz, T. in Proc. SPIE 5165 “X-ray and Gamma-ray Instrumentation for Astronomy XII,” ed. K. Flanagan & O. Siegmund, p.423
- Allen, M. G., Dopita, M. A., Tsvetanov, Z. I., & Sutherland, R. S. 1999, *ApJ*, 511, 686
- Antonucci, R. 1993, *ARA&A*, 31, 473 Pello, R. 2000, *A&A*, 363, 476
- Bianchi, S., Balestra, I., Matt, G., Guainazzi, M., & Perola, G. C. 2003, *A&A*, 402, 141
- Cecil, G., Wilson, A. S., & de Pree, C. 1995, *ApJ*, 440, 181
- Chapman, S. C., Simon, L. M., Alonso-Herrero, A., & Falcke, H. 2000, *MNRAS*, 314, 263
- Cheng, K.-P., et al. 1997, NASA/UIT Team CDROM “UV/Visible Sky Gallery”
- Colbert, E. J. M. 1997, Ph. D. thesis, University of Maryland, College Park
- Colbert, E. J. M., Baum, S. A., Gallimore, J. F., O’Dea, C. P., Lehnert, M. D., Tsvetanov, Z. I., Mulchaey, J. S., & Caganoff, S. 1996a, *ApJS*, 105, 75
- Colbert, E. J. M., Baum, S. A., Gallimore, J. F., O’Dea, & Christensen, J. A. 1996b, *ApJ*, 467, 551
- Colbert, E. J. M., Baum, S. A., O’Dea, C. P., & Veilleux, S. 1998, *ApJ*, 496, 786
- Colbert, E. J. M., Heckman, T., Ptak, A. F., Strickland, D. K., & Weaver, K. A. 2004, *ApJ*, 602, 231
- de Vaucouleurs, G., de Vaucouleurs, A., Corwin, H. G., Buta, R. J., Paturel, G., & Fouque, P. 1991, *Third Reference Catalog of Bright Galaxies (RC3; New York: Springer-Verlag)*
- Dickey, J. M., & Lockman, F. J., 1990, *ARA&A*, 28, 215
- Done, C., Madejski, G. M., & Zycki, P. T. 2003, *ApJ*, 588, 763
- Duc, P.-A., Brinks, E., Springel, V., Pichardo, B., Weilbacher, P., & Mirabel, I. F. 2000, *AJ*, 120, 1238
- Elvis, M., Fasnacht, C., Wilson, A. S., & Briel, U. 1990, *ApJ*, 361, 459
- Fabbiano, G., Zezas, A., & Murray, S. S. 2001, *ApJ*, 554, 1035

- García-Lorenzo, B., Arribas, S., & Mediavilla, E. 2001, *A&A*, 378, 787
- George, I. M., et al. 2002, *ApJ*, 571, 265
- Gilli, R., Maiolino, R., Marconi, A., Risaliti, G., Dadina, M., Weaver, K. A., & Colbert, E. J. M. 2000, *A&A*, 355, 485
- Hardcastle, M. J., Worrall, D. M., & Birkinshaw, M. 1998, *MNRAS*, 296, 1098
- Heckman, T. M. 2004, in “Co-evolution of Black Holes and Galaxies,” (Cambridge Univ. Press), ed. L. Ho, p. 359
- Hummel, E., van Gorkom, J. H., & Kotanyi, C. G. 1983, *ApJ*, 267, L5
- Iwasawa, K., Wilson, A. S., Fabian, A. C., & Young, A. J. 2003, *MNRAS*, 345, 369
- Keel, W. C. 1996, *ApJS*, 106, 27
- Kinkhabwala, A. et al. 2002, *ApJ*, 575, 732
- Malkan, M. A., Gorjian, V., & Tam, R. 1998, *ApJS*, 117, 25
- Moshir, M., et al. 1997, Explanatory Supplement to the IRAS Faint Source Catalog, 1997 update to 1992 version 2 (JPL D-10015), as listed in NED (Pasadena: JPL)
- Mushotzky, R. 1982, *ApJ*, 256, 92
- Mushotzky, R., Marshall, F., Boldt, E., & Serlemitsos, P. 1980, *ApJ*, 235, 377
- Nandra, K., George, I. M., Mushotzky, R. F., Turner, T. J., & Yaqoob, T. 1997, *ApJ*, 476, 70
- Nandra, K., & Pounds, K. 1994, *MNRAS*, 268, 405
- Ogle, P. M., Marshall, H. L., Lee, J. C., & Canizares, C. R. 2000, *ApJ*, 545, L81
- Ogle, P. M., Brookings, T., Canizares, C. R., Lee, J. C., & Marshall, H. L. 2003, *A&A*, 402, 864
- Ptak, A., Serlemitsos, P., Yaqoob, T., Mushotzky, R., & Tsuru, T. 1997, *AJ*, 113, 1286
- Read, A. M., & Stevens, I. R. 2002, *MNRAS*, 335, L36
- Robinson, A. 1989, in “Extranuclear Activity in Galaxies, ed. E. Meurs & R. Fosbury (Garching: ESO), p. 250

- Robinson, A. 1994, *A&A*, 291, 351
- Sako, M. et al. 2002, in “X-ray Spectroscopy of AGN with Chandra and XMM-Newton,” ed. Th. Boller, S. Komassa, S. Kahn, & H. Kunieda (MPE Report no. 279), p. 191
- Sambruna, R. M., et al. 2001, *ApJ*, 546, L13
- Sandage, A., & Bedke, J. 1994, *The Carnegie Atlas of Galaxies* (CIW: Washington)
- Schurch, N. J., Roberts, T. P., & Warwick, R. S. 2002, *MNRAS*, 335, 241
- Smith, R. K., Edgar, R. J., & Shafer, R. A. 2002, *ApJ*, 581, 562
- Soifer, B. T., Neugebauer, G., Matthews, K., Egami, E., & Armus, L. 2004, *PASP*, 116, 493
- Spergel, D. N. et al. 2003, *ApJS*, 148, 175
- Strickland, D. K. 2004, in *The Interplay among Black Holes, Stars, and ISM in Galactic Nuclei*, IAU proc. 222, ed. Storchi-Bergmann, Ho, & Schmitt (Cambridge), p.249
- Strickland, D. K., Heckman, T. M., Colbert, E. J. M., Hoopes, C. G., & Weaver, K. A. 2004a, *ApJS*, 151, 193
- Strickland, D. K., Heckman, T. M., Colbert, E. J. M., Hoopes, C. G., & Weaver, K. A. 2004b, *ApJ*, 606, 829
- Suchkov, A. A., Balsara, D. S., Heckman, T. M., & Leitherer, C. 1994, *ApJ*, 430, 511
- Turner, T. J., & Pounds, K. 1989, *MNRAS*, 240, 833
- Turner, T. J., Weaver, K. A., Mushotzky, R. F., Holt, S. S., & Madejski, G. M. 1991, *ApJ*, 381, 85
- Ulvestad, J. S., & Wilson, A. S. 1989, *ApJ*, 343, 659
- Veilleux, S., Shopbell, P. L., & Miller, S. T. 2001, *AJ*, 121, 198
- Ward, M., Penston, M. V., Blades, J. C., & Turtle, A. J. 1980, *MNRAS*, 193, 563
- Weaver, K. A., Mushotzky, R. F., Serlemitsos, P. J., Wilson, A. S., Elvis, M., & Briel, U. 1995, *ApJ*, 442, 597
- Weaver, K. A., Nousek, J., Yaqoob, T., Mushotzky, R. F., Makino, F., & Otani, C., 1996, *ApJ*, 458, 160

Wehrle, A. E., & Morris, M. 1988, *AJ*, 95, 1689

Wilson, A. S. 1994, in *The Soft X-ray Cosmos: Proc. of the ROSAT Science Symposium*, ed. E. Schlegel & R. Petre (AIP: New York), p. 115

Wilson, A. S., Elvis, M., Lawrence, A., & Bland-Hawthorn, J. 1992, *ApJ*, L75

Yang, Y., Wilson, A. S., & Ferruit, P. 2001, *ApJ*, 563, 124

Young, A. J., Wilson, A. S., & Shopbell, P. L. 2001, *ApJ*, 556,6

Young, A. J., Wilson, A. S., Terashima, Y., Arnaud, K. A., & Smith, D. A. 2002, *ApJ*, 564, 176

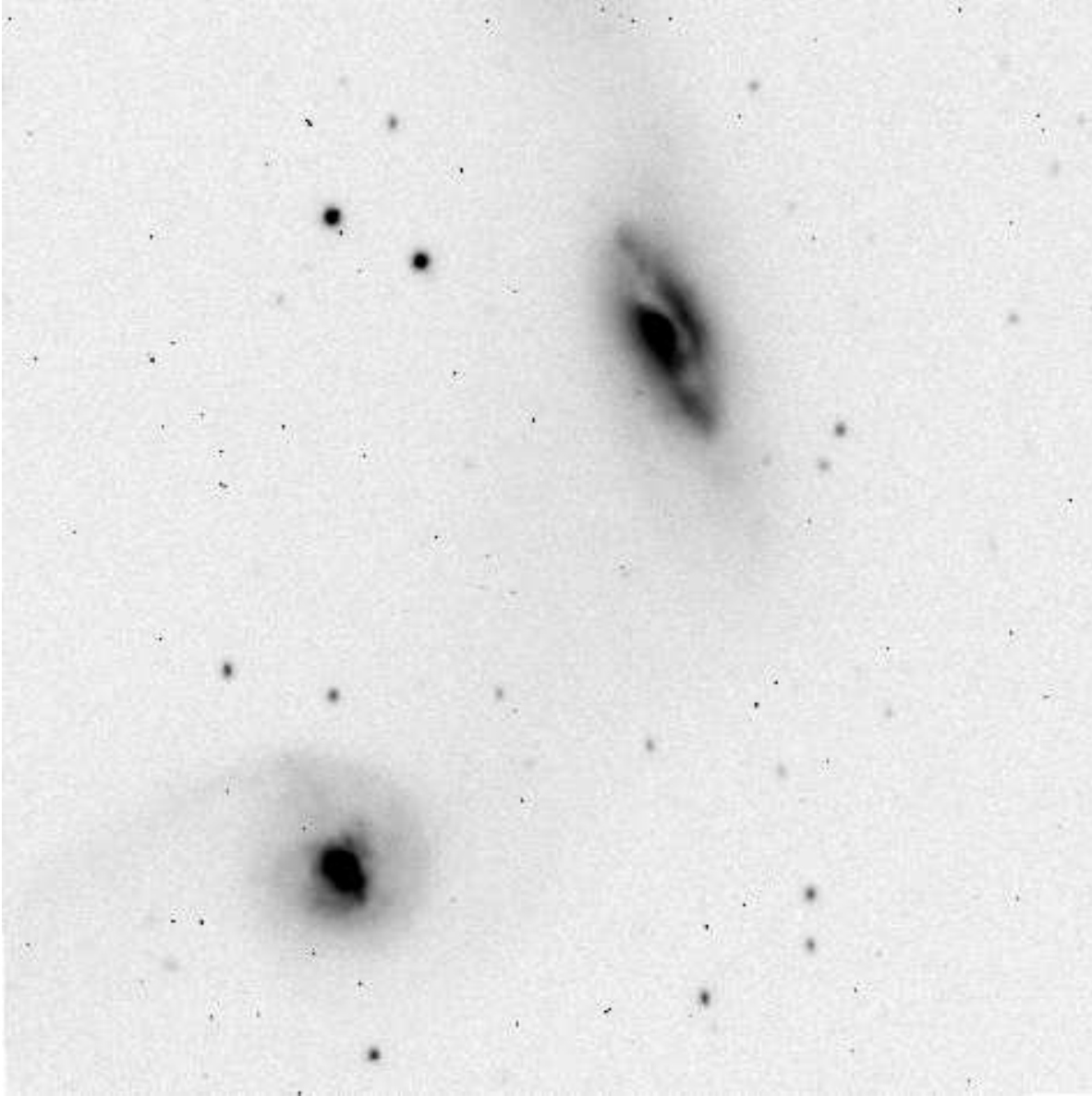


Fig. 1.— Large-scale view of optical (V -band) emission from the galaxy pair NGC 2992/3 (Arp 245) (image from Cheng et al. 1997). North is up, and east is to the left. The FOV is $5.3' \times 5.3'$. Notice the strong dust lane in NGC 2992 (upper right galaxy), and faint tidal tails extending from both galaxies.

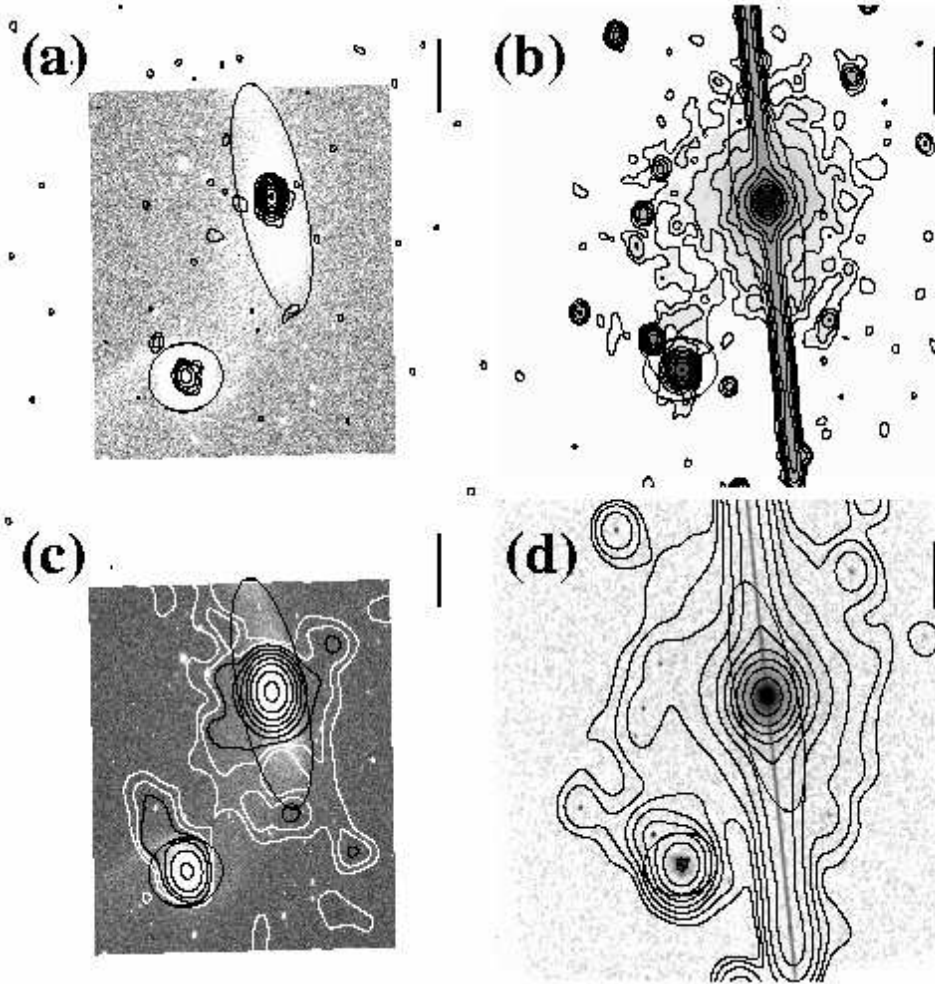


Fig. 2.— Large-scale view of the X-ray Emission from NGC 2992/3. The vertical bars in each panel have size $1'$ (9.5 kpc). The large black ellipses show the extent of NGC 2992 and NGC 2993, using R_{25} and disk axial ratios from RC3 (de Vaucouleurs et al. 1991). Note the CCD readout streak in panels (b) and (d). (a) – Inverted grayscale image of optical V -band emission, with X-ray contours from the combined 1992/1994 ROSAT HRI image (0.2–2.4 keV). The HRI image has been smoothed with a Gaussian kernel of $\sigma = 8$ pixels ($0.''5 \text{ pixel}^{-1}$) so that the final resolution is $\approx 5.''9$ FWHM. The optical image is shown with a log scaling, and the faintest features (e.g., tidal tails) are emphasized. The lowest X-ray contour level ($0.018 \text{ cnts pixel}^{-1}$; $\approx 7 \times 10^{-17} \text{ erg s}^{-1} \text{ cm}^{-2} \text{ arcsec}^{-2}$) was chosen so that the faintest regions of excess over the background level are shown. Contour values increase by a factor of 2.0. (b) – The image and contours are the soft (0.3–2.4 keV) photons from our ACIS observation, smoothed to the same resolution as the ROSAT HRI image. Again, the lowest contour level (coincidentally, also $0.018 \text{ cnts pixel}^{-1}$; $\approx 5 \times 10^{-18} \text{ erg s}^{-1} \text{ cm}^{-2} \text{ arcsec}^{-2}$) was chosen so that only the faintest excess over the CCD background levels are shown. The faintest contours in the figure are from an extended X-ray halo around NGC 2992 and NGC 2993, which may be real, or may be the wings of the PSF from the two nuclear point sources. As in figure (a), contour values increase by a factor of 2.0. (c) – Contours of heavily smoothed ($\sigma = 32$ pixels) ROSAT HRI (0.2–2.4 keV) image. The same optical V -band image is shown here, again with a logarithmic scaling. The grayscale is inverted and the brightest features (e.g. the nuclei) are emphasized. The two white X-ray contours are at 1 and 2 σ levels, while the black contours start at 3σ , and increase by factors of 2 (6, 12, ...). (d) – ACIS full-band (0.3–8.0 keV) image, smoothed with a Gaussian kernel of 2 pixels, with 0.3–2.4 keV ACIS contours to match the resolution of panel (c). All significance levels are computed using the prescription in Hardcastle, Worrall, & Birkinshaw (1998) for $\Sigma^2 \mu \gg 1$, where Σ and μ are the X-ray surface brightness and the mean background rate, respectively.

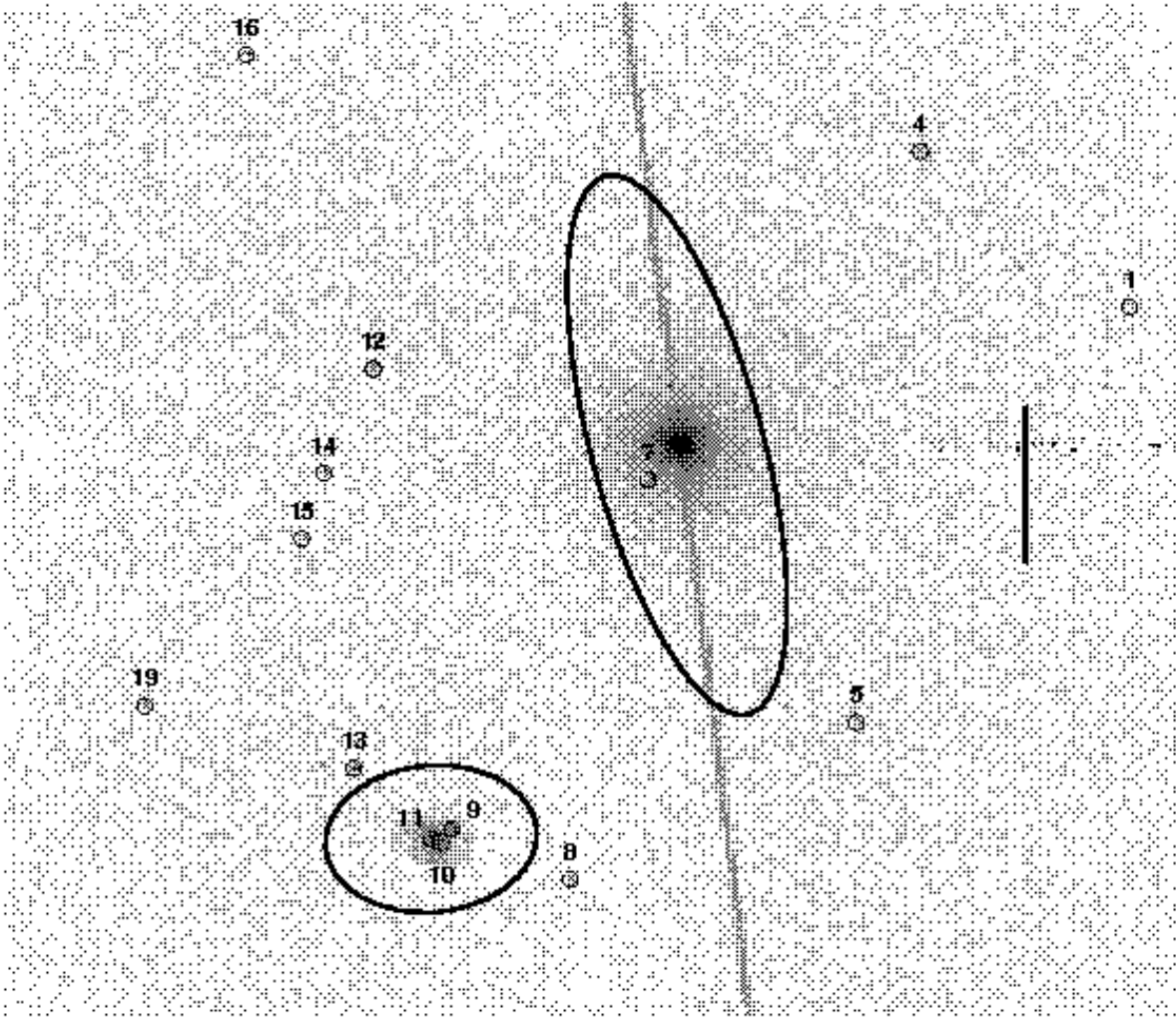


Fig. 3.— X-ray Point Sources in NGC 2992/3. Full-band (0.3–8.0 keV) ACIS image of NGC 2992/3, with positions of X-ray point sources. The sources (see Table 1) are marked with circles of radius $3''$ (for clarity). As in Figure 2, the two black ellipses mark the R_{25} limits (from RC3). The ellipses are centered on the nucleus of NGC 2992, and source 11 in NGC 2993. The scale bar at the right of the image has length $1'$. The nuclear source of NGC 2992 (not labeled) is discussed in detail in section 3.1.2.

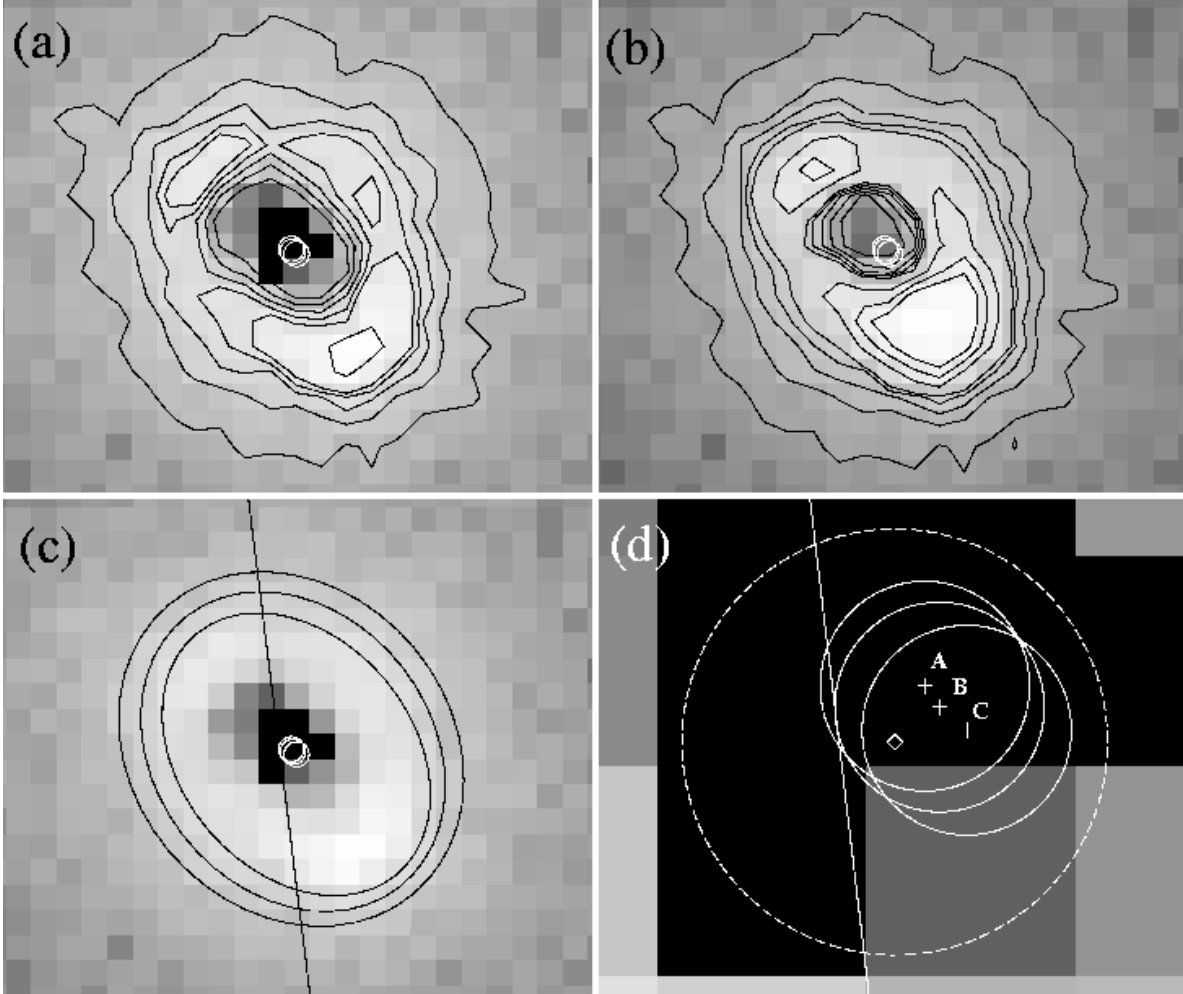


Fig. 4.— Full-band grayscale (inverted) and X-ray contours of the Chandra ACIS X-ray events from the nuclear region of NGC 2992. **(a) and (b)** – The atoll-like structure is created by the rejection of severely piled photon events from the bright nuclear core (i.e., the AGN). Contour levels are 30, 60, 90, 120, 150, 300, 450, and 600 counts pixel⁻¹. Panel (b) shows *all event grades*, including those considered as “bad” for unpiled sources, while panels (a), (c), and (d) show only those events normally considered “good” for unpiled sources (see section 2). A noticeable difference in the two images is apparent above the third contour level (90 counts pixel⁻¹). **(c) and (d)** – The three best-fit ellipses, obtained by fitting the “good” event image, are shown in panel (c). The contour levels for the three ellipses are 51.8, 74.7, and 110.0 counts pixel⁻¹. The centroids of these ellipses are shown in panel (d) by three white circles with $r = 0.''25$, marked A, B, and C, for the inner, middle, and outer ellipse, respectively. The line marks the center of the readout streak. Panel (d) shows a zoom of the central region. The crosses mark the centers of the three ellipses, while the readout streak is shown by a line. Our best estimate for the position of the X-ray core (J2000 9:45:41.95 –14:19:34.8) is marked with a diamond in panel (d), and our best estimate of the uncertainty in the position ($r = 0.''5$) is by the large dashed white circle. For reference, the “middle” ellipse in panel (c) has semi-major and semi-minor axes of $3.4''$ and $2.7''$, respectively, and each pixel shown is $0.492''$. The FOV in panels (a–c) is $11.7'' \times 9.8''$ (1.8×1.5 kpc).

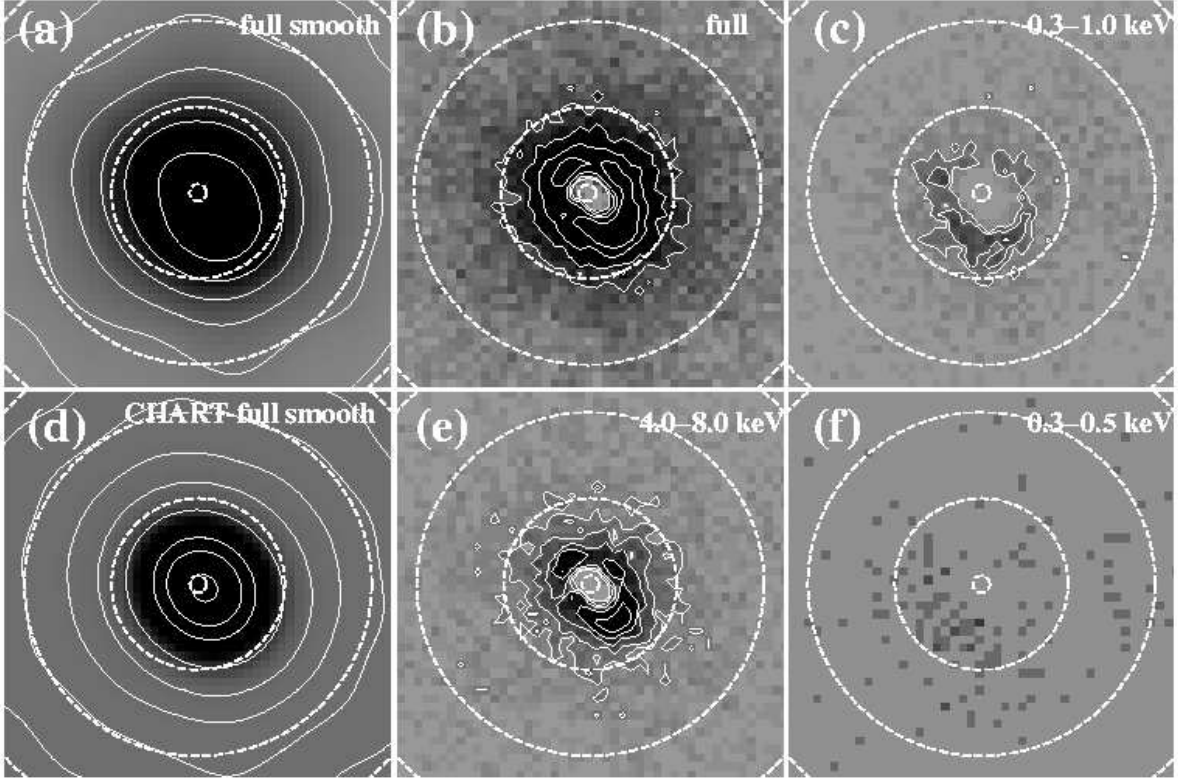


Fig. 5.— Near-nuclear X-ray emission in NGC 2992. Greyscale ACIS images of the nuclear region. Note the extended soft X-ray emission from $\sim 2\text{--}5''$ southeast of the nucleus (source “SE”), in panels (c) and (f). All images are displayed with a log grayscale stretch. The grayscale limits for (a–c) and (e) are -10 to 55 counts pixel $^{-1}$ (1 pixel = $0.''492$). The grayscale limits for the CHART PSF (d) and the very soft image (f) are -3000 to 10000, and -2 to 10 counts pixel $^{-1}$, respectively. Three dashed circles, centered on our best position for the X-ray core (section 3.1.2), are drawn with radii $0.''492$ (1 pixel), $5''$, and $10''$. Panels (b,c) and (e,f) are raw ACIS images in the full (0.3–8.0 keV) energy band, soft (0.3–1.0 keV), hard (4.0–8.0 keV), and very soft (0.3–0.5 keV) energy bands. Panel (a) is the same data as (b), but smoothed with a Gaussian kernel of $\sigma=3$ pixels. Panel (d) is the CHART/MARX simulation for our observation, smoothed with the same Gaussian kernel. The grayscale and contour levels of the CHART PSF were modified to approximately match panel (a). Contour levels for panels (a,b,c,e) start at 2, 16, 4, and 4 counts pixel $^{-1}$ and increase by a factor of 2. Contour levels for the CHART PSF are irregular, so as to approximately match the contours in (a), and to further show the asymmetry of the PSF within $\sim 2''$, where our image is corrupted by pile-up. Those levels are 15, 33, 80, 270, 2500, and 18000, then 36000, and 72000 counts pixel $^{-1}$. The FOV in each panel is $22''$ (3.5 kpc) square.

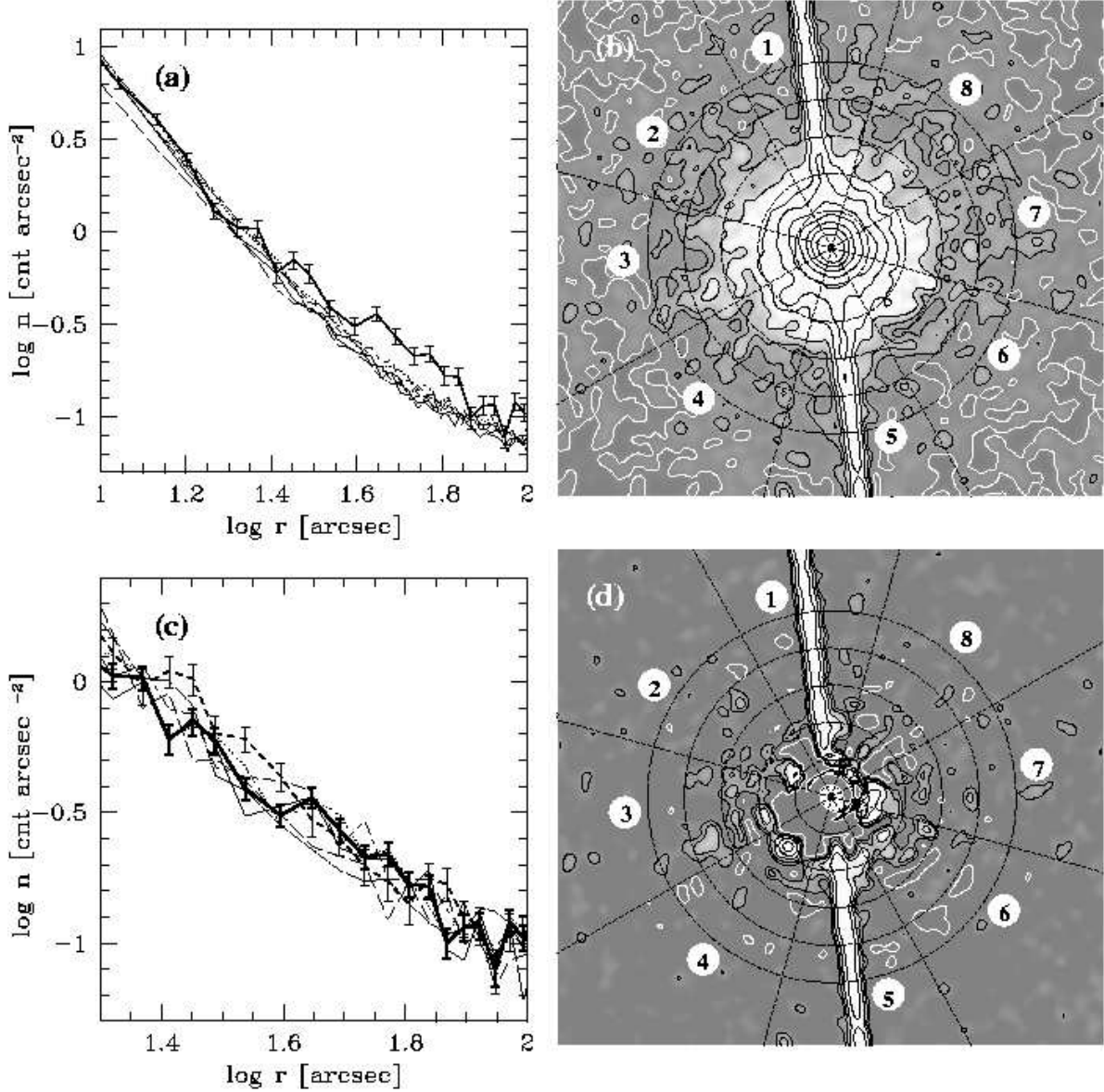


Fig. 6.— Extended X-ray Emission in NGC 2992 (a) The six thin lines are the simulated 0.3–2.4 keV PSF from a CHART/MARX simulation of a point source at the location of the NGC 2992 nucleus. Eight octants are labeled 1–8 in (b) and (d), and octants 2, 3, 4, 6, 7, and 8 are plotted with the following line types: dotted, short dash, long dash, dot/long dash, short dash/long dash, and solid, respectively, in (a) and (c). The thick line is our best PSF, estimated from our Chandra data. (b) Image (inverted linear grayscale) and contours of our 0.3–2.4 keV ACIS image, smoothed with a Gaussian kernel of $\sigma = 1.5''$. Dashed circles are shown at radii spaced $10''$ apart. The white contour level is 0.025 counts pixel $^{-1}$ (the background level), and black contours are $(2^N + 1) \times 0.025$ counts pixel $^{-1}$, where $N \geq 1$. (c) Radial profiles of the 0.3–2.4 keV emission, showing an example of excess in octant 3 (dashed line), from ~ 20 – $40''$ ($10^{1.3}$ – $10^{1.6}$). The thick black line is our best PSF (octants 2+8). The other 5 octants are shown without error bars, although the data have been binned to have ≥ 20 counts per bin, and error bars for all octants are approximately the same. The line types for the octants are the same as for (a). Error bars are Poissonian (\sqrt{N}). (d) PSF-subtracted 0.3–2.4 keV ACIS image. The (inverted) grayscale image is shown with the same linear stretch as in (b), and the dashed circles are the same as for (b). The white contour is -0.05 counts pixel $^{-1}$, and the black contours are 0.05 , 0.1 , 0.2 , 0.4 , and 0.8 counts pixel $^{-1}$. One pixel is $0.''492$ in (b) and (d). Panels (b) and (d) have a FOV of $2.23' \times 2.45'$ (23.3×21.2 kpc).

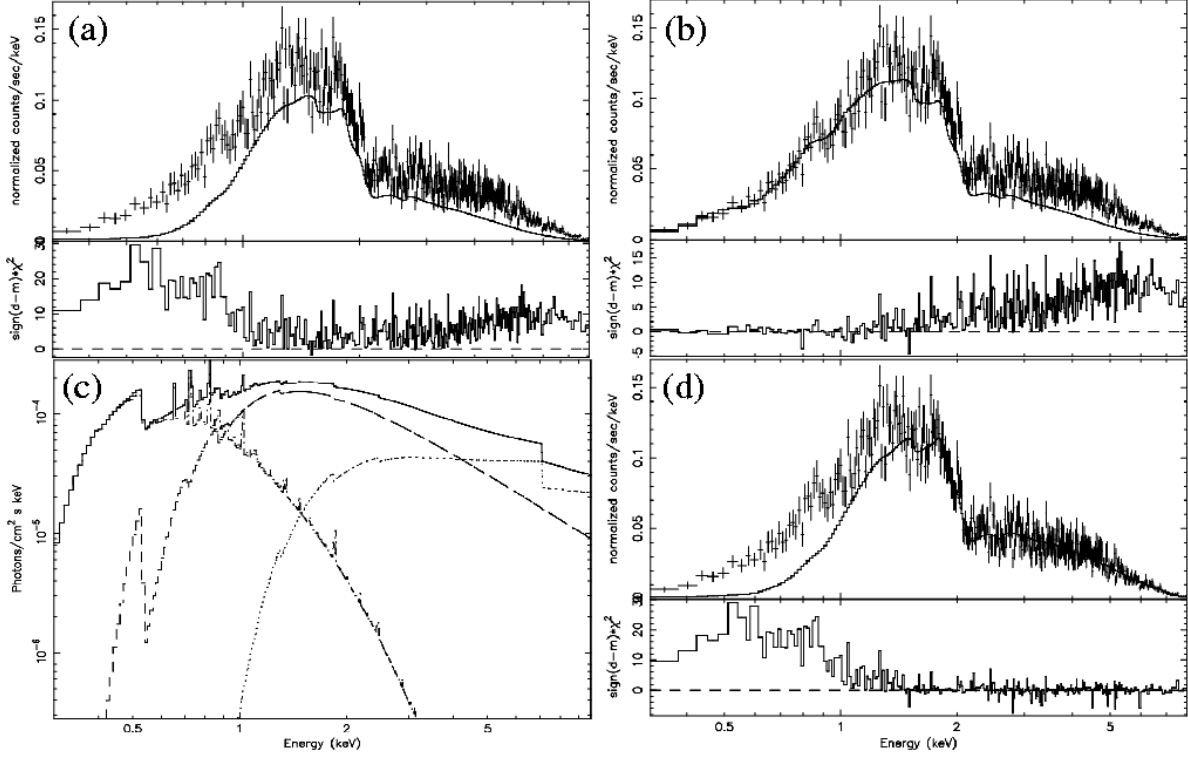


Fig. 7.— The best-fit model (see Table 3, model 3b) for the near-nuclear X-ray spectrum of NGC 2992. Details of the model components (power-law, cold reflection, and thermal plasma) are listed in Table 3. **(a)** Spectral data with AGN power-law model component (in model 3b from Table 3) only, and χ^2 residuals. The “soft excess” residuals $\lesssim 1$ keV are fit with a low-abundance Mekal thermal plasma model, and the hard ($\gtrsim 3$ keV) residuals are fit with a cold reflection model (PEXRAV in XSPEC); **(b)** Spectral data with power-law and Mekal model components, and χ^2 residuals; **(c)** Model components: power-law (dashed), cold reflection (dotted), thermal plasma (dot-dash), and total (solid); **(d)** Spectral data with power-law and PEXRAV components, and χ^2 residuals.

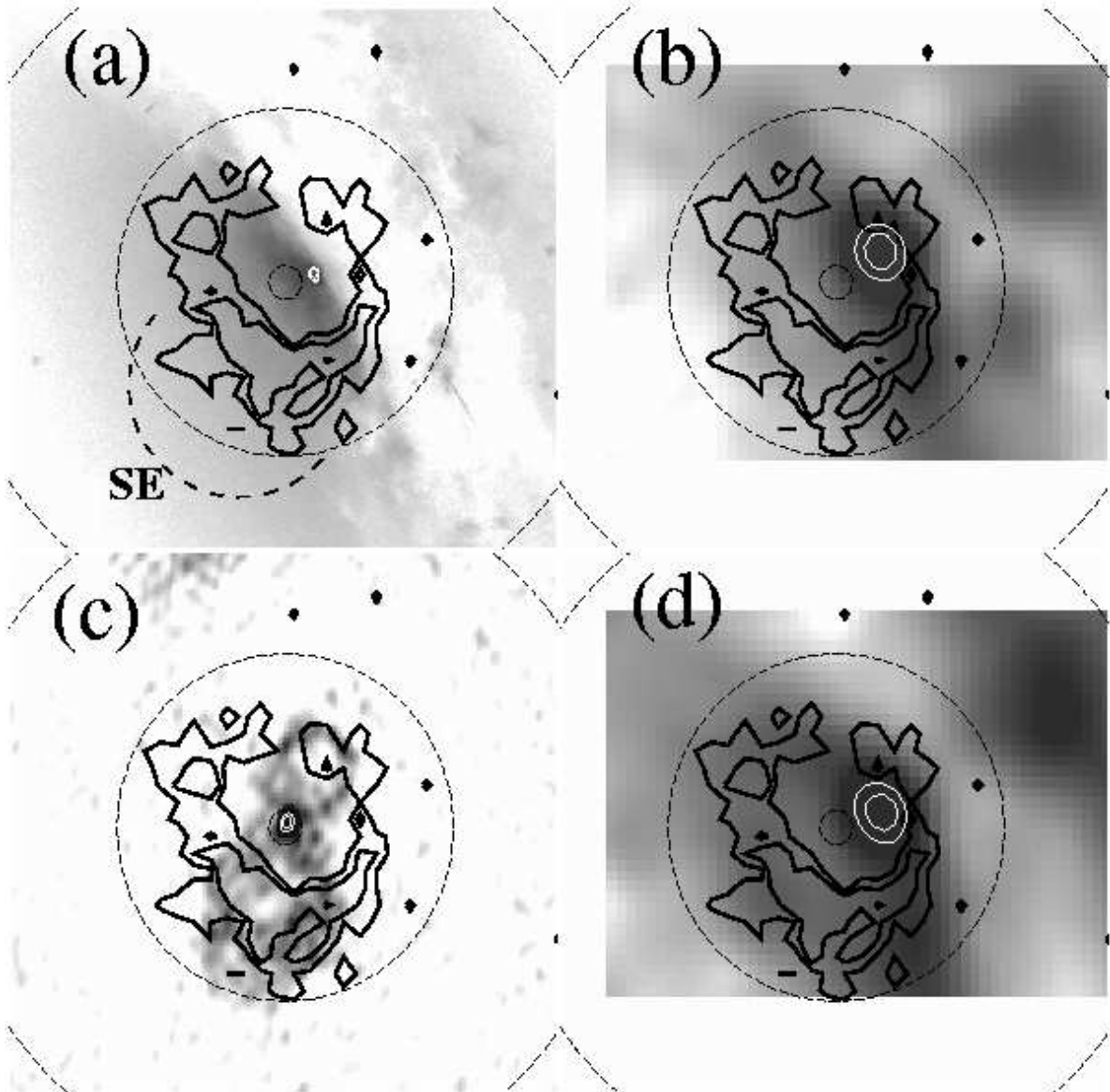


Fig. 8.— Comparison of near-nuclear optical, X-ray and radio emission. Thick black contours in all panels are the 0.3–1.0 keV emission from our ACIS observation. The contours levels are the same as in Figure 5c. The thin white contours show the position of the peak optical and radio emission in the grayscale images (contour levels at 50% and 75% of the peak). The black dashed circles are centered on the position of the X-ray core and have radii of 0.5, 5, and 10". (a) Logarithmically-scaled grayscale image of V-band emission, imaged with the F606W filter on HST (Malkan, Gorjian, & Tam 1998). Note the dust lane to the northwest of the nucleus, running in the northeast-southwest direction. The black dashed semi-circle shows the approximate position of the ‘SE’ X-ray source. (b) Logarithmically-scaled H α image (from Garcia-Lorenzo, Arribas, & Mediavilla 2001). (c) Logarithmically-scaled 6 cm VLA A-configuration image, from Ulvestad & Wilson (1989). (d) Logarithmically-scaled [O III] image (from Garcia-Lorenzo et al. 2001). The astrometry of the HST and VLA images were not modified. The astrometry of the H α and [O III] images from Garcia-Lorenzo et al. was fixed so that the peak of the continuum emission (5100–5150Å) from the same data cube is aligned with the peak in the HST image in panel (a).

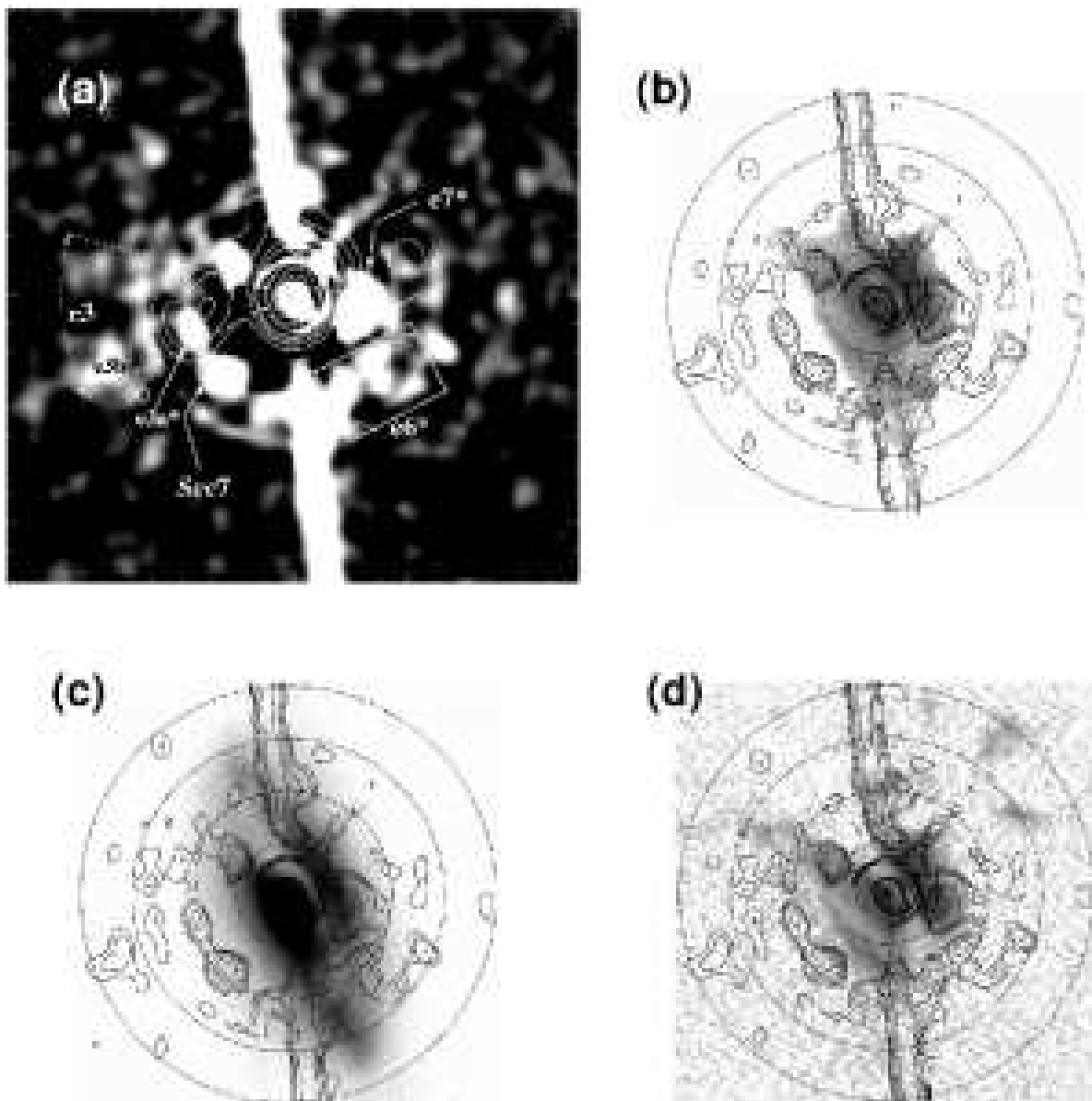


Fig. 9.— Comparison of large-scale optical, X-ray and radio emission. **(a)** Linearly-scaled grayscale image of PSF-subtracted 0.3–2.4 keV X-ray emission (see Figure 6d), with 20 cm radio contours overlaid (from Figure 1 of Hummel et al. 1983). The grayscale is fixed to emphasize low-intensity X-ray emission. Major tick marks are shown every $20''$. X-ray sources $e3$ is outlined by the white dashed region, and the well-defined sources $e3a^*$ and $e3b$ are marked. We also mark point source 7 and the two other well-defined near-nuclear sources $e6^*$ and $e7^*$ (see section 3.1.4). **(b)** Logarithmically-scaled $H\alpha$ image (from Figure 2b of Veilleux, Shopbell & Miller 2001), with contours of X-ray emission (same image as panel a). Contours levels are the same as the black contours in Figure 6d. The dashed circles have radii of 10, 20, 30 and $40''$, as in Figure 6. **(c)** Logarithmically-scaled V-band image (same image as in Figure 1), with contours of X-ray emission, as in panel b. **(d)** Logarithmically-scaled $[O\ III]$ image (from Allen et al. 1999), with contours of X-ray emission, as in panel b.

Table 1. X-ray Point Source Properties

| Src No. | X-ray Position (J2000) | | S/N Ratio | Count Rate (10^{-3} s^{-1}) | F_X (10^{-15} cgs) | L_X ($\log \text{ erg s}^{-1}$) | Notes |
|------------|---------------------------|-------------|--------------|--|-------------------------------------|--|------------------------|
| (1) | (2) | (3) | (4) | (5) | (6) | (7) | (8) |
| 1 | 09:45:30.07 | -14:18:42.1 | 2.4 | 0.8±0.2 | 4.2 | | |
| 2 | 09:45:33.74 | -14:15:26.4 | 17.5 | 5.6±0.4 | 30.2 | | |
| 3 | 09:45:34.33 | -14:16:36.1 | 4.8 | 1.5±0.2 | 8.3 | | |
| 4 | 09:45:35.57 | -14:17:42.7 | 4.5 | 1.4±0.2 | 7.8 | | |
| 5 | 09:45:37.25 | -14:21:20.7 | 3.9 | 1.2±0.2 | 6.7 | (38.9) | |
| 6 | 09:45:39.10 | -14:23:21.4 | 2.1 | 0.7±0.1 | 3.7 | | |
| 7 | 09:45:42.72 | -14:19:48.0 | 5.7 | 1.8±0.4 | 9.8 | 39.1 | ULX in NGC 2992 |
| 8 | 09:45:44.76 | -14:22:20.7 | 2.2 | 0.7±0.1 | 3.8 | (38.7) | |
| 9 | 09:45:47.88 | -14:22:01.5 | 25.7 | 8.2±0.5 | 44.4 | 39.7 | (NGC 2993) |
| 10 | 09:45:48.17 | -14:22:06.5 | 22.0 | 7.0±0.7 | 38.0 | 39.7 | (NGC 2993), (SN2003ao) |
| 11 | 09:45:48.43 | -14:22:05.2 | 30.1 | 9.6±0.7 | 52.1 | 39.8 | (NGC 2993), (SN2003ao) |
| 12 | 09:45:49.95 | -14:19:05.7 | 4.5 | 1.4±0.2 | 7.8 | | |
| 13 | 09:45:50.46 | -14:21:38.3 | 20.5 | 6.6±0.4 | 35.4 | (39.7) | |
| 14 | 09:45:51.25 | -14:19:45.5 | 6.6 | 2.1±0.2 | 11.4 | | |
| 15 | 09:45:51.83 | -14:20:10.6 | 2.4 | 0.8±0.1 | 4.1 | | |
| 16 | 09:45:53.29 | -14:17:05.4 | 9.1 | 2.9±0.3 | 15.7 | | |
| 17 | 09:45:53.46 | -14:23:55.5 | 2.1 | 0.7±0.1 | 3.7 | | |
| 18 | 09:45:53.77 | -14:23:57.1 | 2.2 | 0.7±0.1 | 3.9 | | |
| 19 | 09:45:55.96 | -14:21:14.4 | 7.7 | 2.5±0.2 | 13.4 | | |
| 20 | 09:45:56.64 | -14:24:18.2 | 4.6 | 1.5±0.2 | 7.9 | | |

Notes on table columns: (1) Source number; (2,3) Right Ascension and Declination of X-ray source, taken from XASSIST output (URL:WWW.XASSIST.ORG); (4) XASSIST signal-to-noise ratio; (5) ACIS count rate and error in count rate, in the 0.3–8.0 keV band; (6) Observed X-ray flux in the 0.3–8.0 keV band, assuming a simple absorbed power-law with $\Gamma = 1.8$ and the Galactic hydrogen absorption column ($5.26 \times 10^{20} \text{ cm}^{-2}$, Dickey & Lockman 1990). Units are $10^{-15} \text{ erg s}^{-1} \text{ cm}^{-2}$; (7) Logarithm of observed X-ray luminosity, assuming a distance of 32.5 Mpc, for point sources within the R_{25} ellipses of NGC 2992 and NGC 2993. Values in parentheses are for sources 5, 8, and 13, which are positioned outside the R_{25} ellipses but within ellipses corresponding to $R=2R_{25}$; (8) Notes. The SIMBAD sources within $10''$ of the X-ray position are listed in parentheses (centers of NGC2992 and NGC2993, and SN2003ao).

Table 2. Kiloparsec-scale Extended Soft X-ray Emission near NGC 2992

| Octant/ Range(") | Source Name | Counts in Energy Band | | | | | | L_X 0.3–8.0 keV | Notes |
|---------------------|----------------|-----------------------|-------------|-------------|-------------|-------------|-------------|----------------------|--------------------------------|
| | | 0.3–1.0 keV | 1.0–1.5 keV | 0.3–1.5 keV | 1.5–2.4 keV | 0.3–2.4 keV | 2.4–8.0 keV | | |
| (1) | (2) | (3) | (4) | (5) | (6) | (7) | (8) | (9) | (10) |
| 1 | ... | ... | ... | ... | ... | ... | ... | ... | CCD readout streak |
| 2 | ... | ... | ... | ... | ... | ... | ... | ... | no significant excess |
| 3/20–40" | e3 | <22 | 26±12 | 45±15 | 43±15 | 90±22 | <74 | 38.86 | |
| 4/15–25" | Src7 | 17±7 | 23±11 | 51±13 | 35±14 | 82±19 | <60 | 38.82 | point-like (source 7, Table 1) |
| 5 | ... | ... | ... | ... | ... | ... | ... | ... | CCD readout streak |
| 6/15–30" | e6 | <24 | <35 | <44 | 57±16 | 75±22 | <70 | 38.78 | |
| 7/10–20" | e7 | 42±12 | <40 | 64±18 | <49 | 74±24 | <72 | 38.78 | |
| 8 | ... | ... | ... | ... | ... | ... | ... | ... | no significant excess |
| ... | e3a* | ... | ... | ... | ... | 22±6 | ... | 38.25 | see Fig 9 |
| ... | e3b | ... | ... | ... | ... | 31±7 | ... | 38.40 | see Fig 9 |
| ... | e6* | ... | ... | ... | ... | 83±10 | ... | 38.83 | see Fig 9 |
| ... | e7* | ... | ... | ... | ... | 94±11 | ... | 38.88 | see Fig 9 |

Excess net X-ray counts in various energy bands, using our best PSF, which was generated from regions 2 and 8 (see Figure 3). For reference, at 32.5 Mpc, 10" is 1.58¹ kpc. Only regions with significant ($>2\sigma$) excess counts in one of the bands are reported here. where σ is the sum (in quadrature) of the Poisson errors (\sqrt{N}) of the net counts for the given region, from the data and from the PSF. Upper limits are given as 3σ . For reference, the exposure time is 49.5 ks. Notes on table columns: (1) Octant (see Figure 3), and radial range in arcseconds; (2) Source name, (3–8) Counts in ACIS Energy Bands; (9) Full-band (observed/absorbed) X-ray luminosity in units of \log erg s⁻¹, scaled from the 0.3–2.4 keV count rate, assuming a Bremsstrahlung emission model with $kT=0.5$ keV and the Galactic absorption column 5.26×10^{20} cm⁻². To convert observed 0.3–8.0 keV X-ray luminosities to observed luminosities in the ROSAT (0.2–2.4 keV) band, multiply by 1.02. (10) Additional notes.

Table 3. Model Fits to Near-nuclear X-ray Spectrum of NGC 2992

| — Model — | χ^2_ν | χ^2/dof | L_X^{obs} | F_X^{unabs} | Γ/kT | N_H | Norm | Additional Notes | |
|-----------|------------------------------------|--------------|-------------|---------------|-------------|-----------------------------------|--------------------------|------------------------|-----------------------------|
| No. | Description | (3) | (4) | (5) | (6) | (7) | (8) | (9) | (10) |
| (1) | (2) | | | (log cgs) | | | (10^{22} cm $^{-2}$) | (10^{-4}) | |
| 1a | PL | 1.13 | 401.1/355 | 41.55 | -11.29 | $\Gamma = 0.91 \pm 0.02$ | 0.19 ± 0.04 | $3.21^{+0.17}_{-0.15}$ | |
| 1b | PL(fixed) | 3.74 | 1331.6/356 | 41.70 | -11.36 | $\Gamma = 1.86f$ | 0.73 | 9.33 | |
| 2a | PL+PL (Part Cov) | 1.05 | 371.7/354 | 41.16 | -11.68 | $\Gamma_1 = 1.86f$ | 0.71f | $3.71^{+0.40}_{-0.33}$ | |
| | | | | 41.56 | -11.53 | $\Gamma_2 = 0.52^{+0.12}_{-0.05}$ | $0.008 (<0.059)$ | $1.25^{+0.39}_{-0.12}$ | |
| 2b | PL+ PEXRAV | 1.18 | 419.0/354 | 41.37 | -11.47 | $\Gamma = 1.86f$ | 0.71f | 5.93 ± 0.33 | |
| | | | | 41.42 | -11.65 | | 0.061 ± 0.028 | $0.77^{+0.18}_{-0.17}$ | R= 198^{+38}_{-35} |
| 2c | PL+ Mekal $_\odot$ | 2.82 | 997.4/354 | 41.54 | -11.30 | $\Gamma = 1.86f$ | 0.71f | 8.99 | Z=1.0fZ $_\odot$ |
| | | | | 39.82 | -13.12 | kT=0.25 | 0 | 0.36 | |
| 2d | PL+ Mekal $_{VarAb}$ | 2.80 | 989.6/353 | 41.54 | -11.30 | $\Gamma = 1.86f$ | 0.71f | 8.96 | |
| | | | | 39.86 | -13.06 | kT=0.27 | 0 | 2.25 | Z= 0.12Z $_\odot$ |
| 3a | PL+ PEXRAV+ Mekal $_\odot$ | 1.11 | 390.0/351 | 41.43 | -11.43 | $\Gamma = 1.86f$ | 0.71f | $6.85^{+0.15}_{-0.23}$ | |
| | | | | 41.35 | -11.74 | | 0 (<0.034) | $1.83^{+1.56}_{-0.98}$ | R= 785^{+875}_{-355} |
| | | | | 39.66 | -13.21 | kT=0.31 $^{+0.04}_{-0.03}$ | 0.04 (<0.08) | $0.27^{+0.30}_{-0.11}$ | Z=1.0fZ $_\odot$ |
| 3b | PL+ PEXRAV+ Mekal $_{VarAb}$ | 1.03 | 361.4/350 | 41.39 | -11.45 | $\Gamma = 1.86f$ | 0.71f | $6.3^{+0.9}_{-2.7}$ | |
| | | | | 41.36 | -11.48 | | $2.90^{+2.33}_{-1.09}$ | $3.7^{+1.5}_{-1.1}$ | R= 28^{+16}_{-10} |
| | | | | 40.16 | -12.53 | kT=0.51 $^{+0.26}_{-0.19}$ | $0.12^{+0.27}_{-0.08}$ | $8.8^{+21}_{-5.2}$ | Z=0.013 (<0.026) Z $_\odot$ |

See section 3.2.2 for description of the “near-nuclear” region used to extract the spectrum. All fits include an additional Galactic Hydrogen absorption column of 5.26×10^{20} cm $^{-2}$ (Dickey & Lockman 1990). The letter “f” after the value indicates that the parameter was fixed at that value during the fit. XSPEC parameter errors were not computed for poorly fit models 1b, 2c, and 2d, which all had $\chi^2_\nu > 2.5$. All errors are given for 90% confidence for one interesting parameter ($\Delta\chi^2 = 2.7$).

Notes on table columns: (1) Model Number; (2) Description of XSPEC model (PL = power law, PEXRAV = cold reflection of a PL spectrum, Mekal = thermal plasma, VarAb = Non-solar variable abundance); (3,4) Reduced chi-square value $\chi^2_\nu = \chi^2/\nu$, where ν is the number of degrees of freedom (dof); (5) Logarithm of the observed 0.3–8.0 keV X-ray luminosity of the component in erg s $^{-1}$ (assuming D=32.5 Mpc); (6) Logarithm of the *unabsorbed* 0.3–8.0 keV X-ray flux of the components. All N_H values were zeroed. (7) Photon index Γ for PL and PEXRAV models, or Mekal plasma temperature in keV; (8) “Intrinsic” Hydrogen absorption column of model component, in units of 10^{22} cm $^{-2}$; (9) XSPEC Model Normalization. For the PL and PEXRAV models, the units are photons s $^{-1}$ cm $^{-2}$ keV $^{-1}$ at 1 keV. For the PEXRAV model, the normalization is for the direct component only. For the Mekal model, the units are $10^{-14}/(4\pi D^2) \int n_e(n_H/1 \text{ cm}^3)dV$, where D is the distance to the X-ray source in cm; (10) Additional Notes on component parameters. R is the reflection scaling factor for the PEXRAV model. The e -folding energy for the PEXRAV model was fixed at 100 keV.